J. Mech. Phys. Solids 171 (2023) 105136

Contents lists available at ScienceDirect

Journal of the Mechanics and Physics of Solids

journal homepage: www.elsevier.com/locate/jmps

Theory of hard magnetic soft materials to create magnetoelectricity

Amir Hossein Rahmati [a], Rong Jia [b], Kai Tan [b], Xuanhe Zhao [c], Qian Deng [d], Liping Liu [e,*], Pradeep Sharma [a,*]

[a] Department of Mechanical Engineering, University of Houston, Houston, TX 77204, USA
[b] State Key Laboratory for Strength and Vibration of Mechanical Structures, School of Aerospace Engineering, Xi'an Jiaotong University, Xi'an 710049, China
[c] Department of Civil and Environmental Engineering, Massachusetts Institute of Technology, Cambridge, MA 02139, USA
[d] Department of Engineering Mechanics, School of Aerospace Engineering, Huazhong University of Science and Technology, Wuhan, 430074, China
[e] Department of Mathematics, Rutgers University, NJ 08854, USA

ARTICLE INFO

Keywords:
Soft material
Magnetoelectricity
Hard magnetic soft electrets
Programmed hard magnetic soft electrets
Magnetoelectric voltage coupling coefficient

ABSTRACT

Materials that generate electrical signals upon exposure to a well-controlled stimuli are high desirable. In that context, magnetoelectrics are unusual in the sense that the stimulus may be applied remotely (and wirelessly) without recourse to any physical contact. Wireless energy harvesting, remotely triggered biomedical agents, soft robots among others are some of the applications of such materials. The magnetoelectric property however is somewhat elusive in natural materials and artificial composites designed to exhibit this effect are invariably hard materials, require a pre-existing magnetic field and only exhibit a non-trivial coupling at high frequencies. Our recent experiments (presented elsewhere) demonstrated a facile route to create highly deformable soft magnetoelectric materials predicated on the concept of programmable hard magnetic soft materials with embedded immobile electric charges (electrets). In this work, we offer a nonlinear theoretical framework to both understand the emergent magnetoelectric effect in this class of soft materials as well as to design novel structures and devices with tailored functionality. Specifically, we are able to show that mechanical strain convects residual electrical and magnetic field states to mediate an unprecedented strong magnetoelectric coupling that is independent of the applied external magnetic field and retains its potency at low frequencies. We analytically solve simple illustrative examples to establish insights and present a finite element approach to handle complexities that may be otherwise intractable. The predictions of our theory agree very well with published experiments.

1. Introduction

There are several compelling reasons to develop magnetoelectric (ME) materials. Such materials enable extremely low power memories where data is written electrically but read magnetically (Bibes and Barthélémy, 2008). Electrical energy may be harvested simply by the remote application of a magnetic field, which may be used for wireless charging of small-scale devices or sensing (Annapureddy et al., 2017). In a rather fascinating recent study, hollow magnetoelectric capsules were used for drug delivery. Upon suitable application of a magnetic field, nano-electroporation mediated release of drugs at cancer sites was achieved (Guduru

* Corresponding authors.
E-mail addresses: psharma@uh.edu (P. Sharma), liu.liping@rutgers.edu (L. Liu).

https://doi.org/10.1016/j.jmps.2022.105136
Received 25 September 2022; Received in revised form 7 November 2022; Accepted 11 November 2022
Available online 21 November 2022
0022-5096/© 2022 Elsevier Ltd. All rights reserved.

et al., 2013). We remark that biological media is transparent to magnetic fields and thus is of special relevance for biomedical applications.[1]

Naturally occurring single-phase ME materials are scarce and the reason is simple. Such materials must couple magnetic order parameter (typically found in a class of metals) with electrical polarization order (found in certain types of dielectrics). This contradictory requirement and other associated details (see Schmid, 1994; Hill, 2000 for further information) imply that the discovered single phase natural ME's, aside from being rare, have an exceedingly low coupling; especially at temperature range typically associated with engineering applications (Bhoi et al., 2021). A survey of research activities in the field of multiferroics (which are magnetoelectric) can be found in several review articles (Dong et al., 2015; Catalan and Scott, 2009; Spaldin and Ramesh, 2019; Lottermoser et al., 2004; Wang et al., 2010; Pyatakov and Zvezdin, 2012; Tokura et al., 2014; Fiebig et al., 2016; Eerenstein et al., 2006).

An expedient route to design magnetoelectrics has been by creating composites composed of magnetostrictive (ferromagnetic) and piezoelectric (ferroelectric) constituents. The emergent ME effect in such composites is due to the cross coupling between magnetostrictive and piezoelectric phases and is (usually) mediated through mechanical deformation. The strain generated in the magnetostrictive phase of the composite, in response to applied magnetic field, is transferred to piezoelectric phase through the interface of the two phases and the developed strain in the piezoelectric phase generates electrical polarization. Such composites, like single phase magnetoelectrics are rather *hard* materials and earlier studies reported magnetoelectric voltage coupling coefficients that did not surpass 0.1 $\mathrm{Vcm^{-1}Oe^{-1}}$ (Zhou et al., 2015; Nan et al., 2008).[2] In early 2000s, theoretical (Nan et al., 2001b,a) and experimental (Ryu et al., 2001b,a; Dong et al., 2003) research confirmed the existence of giant ME effect (with the voltage coupling coefficient greater than 1 $\mathrm{Vcm^{-1}Oe^{-1}}$), in composites containing magnetostrictive rare-earth-iron alloy Tb1–xDyxFe2 (Terfenol-D). This observation made these composites desirable for technological applications. Further research into the development of magnetoelectric composites have enabled giant ME effect in different composites which contain polymer or ceramic as piezoelectric phase and a variety of magnetostrictive materials, including ferrites (Srinivasan et al., 2003), Fe–Ga alloy (Dong et al., 2005) and Metglas (Zhai et al., 2006). We refer the reader to several reviews for a survey of the research on this topic (Ma et al., 2011; Liang et al., 2021; Narita and Fox, 2018; Hu et al., 2017; Chu et al., 2018; Malley et al., 2021; Pradhan et al., 2020; Martins and Lanceros-MenNdez, 2013; Bitla and Chu, 2018).

Notwithstanding the progress made on the subject of magnetoelectrics, especially in the context of composites, we reiterate that soft magnetoelectrics are rather elusive. Soft materials capable of large elastic deformation offer new functionalities that is simply not possible with their hard counterparts—e.g soft robotics, health care (Cianchetti et al., 2018), stretchable, flexible and wearable electronics (Rogers et al., 2010) among others. We remark that although there have been successful attempts in creating materials for power harvesting from different sources of energy including mechanical (Dagdeviren et al., 2014), thermal (Peng et al., 2019), chemical (Shi et al., 2018) or optical (de Cea et al., 2021), surprisingly limited progress has been made in the development of soft materials suitable for magnetoelectric conversion despite all the advantages it could potentially offer.

There are several other disadvantages that plague the current state-of-the-art in composite magnetoelectrics:

- The design and fabrication of ME composites is a complex process as there are a large number of factors including connectivity, microstructure, volume fraction of individual phases, among others (Liang et al., 2021) that must be carefully tailored to achieve a large ME effect and avoid problems such as current leakage and substrate clamping (Ma et al., 2011). The ME coupling in these materials strongly depends on the strain transfer between the different phases and this aspect is not simple to control (Pradhan et al., 2020).
- A key disadvantage of the current high quality ME composites are that they are not mechanically soft. Polymer based composites which, compared to ceramic and magnetic alloy based composites, offer some recourse however the ones created so far (see Bitla and Chu, 2018 and references therein) are thin materials that can accommodate deformations similar to bending in which deflection may be quite large but strain is small. This is partially because truly soft piezoelectric materials do not exist. Appreciable intrinsic piezoelectricity only exists in hard brittle materials with non-centrosymmetric crystals (Liang et al., 2021; Deng et al., 2014a; Rahmati et al., 2019; Deng et al., 2014b). Although some polymers such as PVDF and its co-polymers exhibit piezoelectricity in their semi-crystalline phase, the magnitude of their stiffness is in the range of GPa which is not considered soft enough (Bhavanasi et al., 2016; Lu et al., 2020; Liu et al., 2018; Chang et al., 2010).
- Another significant disadvantage of ME composites is that a static bias magnetic field is required for the composites to exhibit a significant coupling. As mentioned earlier, the ME coupling in composites is realized through the so-called "product property" of the two piezoelectric and magnetoelastic phases. The magnetic field induced strain generated in the magnetoactive phase is transferred to the piezoelectric which leads to the generation of an electric signal. The strain or stretch developed in a magnetostrictive material depends quadratically on the external magnetic field. Thus, the ME coupling coefficient of the material (which is related to the rate of change of strain with respect to external magnetic field) depends *linearly* on the external magnetic field. Therefore, the magnetoelectric coefficient of the composites depends on the applied external field and is asymptotically zero as the applied field diminishes. Accordingly, an additional external applied static bias magnetic field is necessary to achieve a non-trivial magnetoelectric coupling in composites. This places requirements of additional weight and space (Palneedi et al., 2018) rendering any sort of miniaturization difficult. We remark that, in the past decade, notions of

[1] A fact we rely on in medical equipment like magnetic resonance imaging where human bodies can be subjected to very high-strength magnetic fields. An analogous exposure to electrical fields, of course, would be fatal.

[2] The magnetoelectric voltage coefficient links the change in electric field with respect to the magnetic field.

introducing internal/self-bias field in composite to replace the external bias field have been proposed (Mandal et al., 2010, 2011; Gong et al., 2019; Zhang et al., 2013; Lage et al., 2012). However, most self-biased composites are bulky in size and their fabrication requires special synthesis process which leads to additional steps in developing functional devices (Zhou et al., 2015).

- Typical ME composites exhibit a strong coupling only at high frequencies and their coupling coefficient significantly diminishes at small frequencies. This is unfortunate since many applications such as targeted drug delivery (Nair et al., 2013), brain stimulation (Nguyen et al., 2021), tissue regeneration and wireless energy transfer for implantable medical devices require lower frequency (since high frequency magnetic field may cause safety concerns) (Kopyl et al., 2021).

Recently, we have proposed a new mechanism to create magnetoelectric coupling using soft materials like rubber and without the need for piezoelectric and magnetostrictive materials (Alameh et al., 2014; Tan et al., 2020a). The central idea is to embed immobile charges or dipoles in a soft material (—such materials are called electrets) and ensure that the magnetic permeability of the material is higher than that of vacuum (by introducing a modest fraction of magnetic particles that do not appreciably alter the mechanical stiffness). We showed both theoretically (Alameh et al., 2014) and experimentally (Tan et al., 2020b) that these soft-magnetic soft electret(SMSE) materials exhibit a ME effect. The mechanism underpinning such materials is predicated on the fact that electrets exhibit a significant artificial piezoelectric-like behavior (Rahmati et al., 2019; Deng et al., 2014a,b; Liu and Sharma, 2018; Apte et al., 2020; Bauer et al., 2004; Rahmati et al., 2022). Based on the Maxwell stress effect, any material with relative permeability greater than one will deform in response to an external magnetic field. A non-uniform deformation in the electret materials can lead to a piezoelectric effect. Therefore, a ME effect can be seen in SMSEs made of two different layers with different material properties. To the best of our knowledge, soft SMSEs are the only soft ME "*materials*" developed so far, even though there is precedent of ME coupling in soft "*structures*" through embedding multiferroic nanoparticles in soft materials (Nair et al., 2013; Mushtaq et al., 2019; Zhang et al., 2021b; Dong et al., 2020) or through electromagnetic induction (Zhang et al., 2020, 2021a).

Despite the progress made recently in the context of soft magnetoelectric materials (summarized in the preceding paragraph), the ME coupling itself is rather small unless extraordinarily large magnetic fields are applied. This is because the relationship between magnetic field and strain induced as a result of the Maxwell stress is quadratic in SMSE materials. In this sense, SMSEs behave similar to magnetoelectric composite materials where a bias magnetic field is required to achieve strong magnetoelectric coupling. Furthermore, since there is a quadratic relationship between strain developed in the material and applied magnetic field, the SMSEs are not sensible to the direction of applied magnetic field and the ME response only depends on the magnitude of the applied field. This restricts application of SMSEs as magnetoelectric sensors. Moreover, non-uniform strain is required to achieve a large magnetic effect under uniform magnetic field in SMSEs and it is not straightforward to induce non-uniform strain without an elastic mismatch.

A recent development pertaining to a novel class of magnetosensitive materials present an alternative solutions to create soft materials that exhibit large actuation strains. Zhao et al. used soft elastomers with embedded high-coercivity hard-magnetic microparticles (Zhao et al., 2019; Kim et al., 2018). A high remnant residual flux density allows them to exhibit a linear relationship between strain and magnetic field. Using the notion of programming the pattern of magnetic dipoles, tailored magnetic actuation can be achieved and remarkable experimental and theoretical results have been reported in a rather short time. We remark that the recent literature has exploded with clever design of magneto-mechanical materials and attendant applications (Wu et al., 2020; Kuang et al., 2021; Ze et al., 2020, 2022; Wu et al., 2022; Danas et al., 2012; Danas and Triantafyllidis, 2014; Lefèvre et al., 2017; Danas and Triantafyllidis, 2014; Mukherjee et al., 2020, 2021; Psarra et al., 2019; Lefèvre et al., 2020)

In this work, we present a mathematical theory that combines the concept of hard magnetic soft materials with electrets (HMSE). Like in prior works, the magnetic dipoles can be programmed—which we will refer to as programmable hard magnetic soft electrets(PHMSEs). Thus HMSEs are dielectric materials with immobile residual electric charges/dipoles and residual magnetic flux density(Fig. 1). The magnetoelectric effect will emerge in HMSEs if the magnetic field generates a non-uniform strain in the material. We present a nonlinear coupled theory for the behavior of HMSEs. We also present a finite element (FE) implementation of the theory. Similar to SMSEs, the simplest possible geometry for HMSEs is composed of a bi-layer with an elastic mismatch or/and differing magnetic flux density with a layer of external charges at the interface. Moreover, as it is quite simple to program residual flux density of hard magnetic soft materials to exhibit a desired form of deformation (Gong et al., 2020), we propose PHMSEs in which non-uniform strain is generated in response to a uniform external magnetic field due to presence of gradient in the residual magnetic flux density in the elastically homogeneous soft material. Since bending deformation yields lower resonance frequency and large strain gradient, we design a PHMSE with the residual magnetic flux density tailored to obtain bending deformation in response to a uniform magnetic field. We show that the bending deformation mediated coupling in HMSEs can lead to a remarkably strong magnetoelectric effect. We find excellent agreement between our theoretical predictions and experimental realization of both HMSEs and PHMSEs. As an aside, we also take the opportunity to rigorously justify some of the approximations used in past work and comment on the symmetry property of the Cauchy stress tensor in the context of hard magnetic soft materials.

This paper is organized as follows. Theoretical study of the HMSEs is presented in Section 2. The governing equation and boundary conditions required to analyze behavior of the HMSEs is presented in Section 2.1 using a variational approach. In particular, in Section 2.2, we revisit an issue that often is discussed int he context of magnetic materials—the symmetry of the Cauchy stress tensor. A simple finite element implementation for incompressible HMSEs is presented in Section 3. The voltage coupling coefficient for a bi-layer HMSE is determined analytically in Section 4.1. An approximate estimate for the voltage coupling coefficient enabled through magnetic field induced bending deformation of a HMSE is obtained in Section 4.2. We elaborate on shape programmable feature of HMSE materials in Section 4.3. In Section 5, we present numerical results for cases that are intractable analytically. We demonstrate the prospect of wireless energy harvesting using a parallel plate capacitor made of hard magnetic soft material in Section 5.2. The behavior of a PHMSE under magnetic field induced bending is studied in Section 5.3.

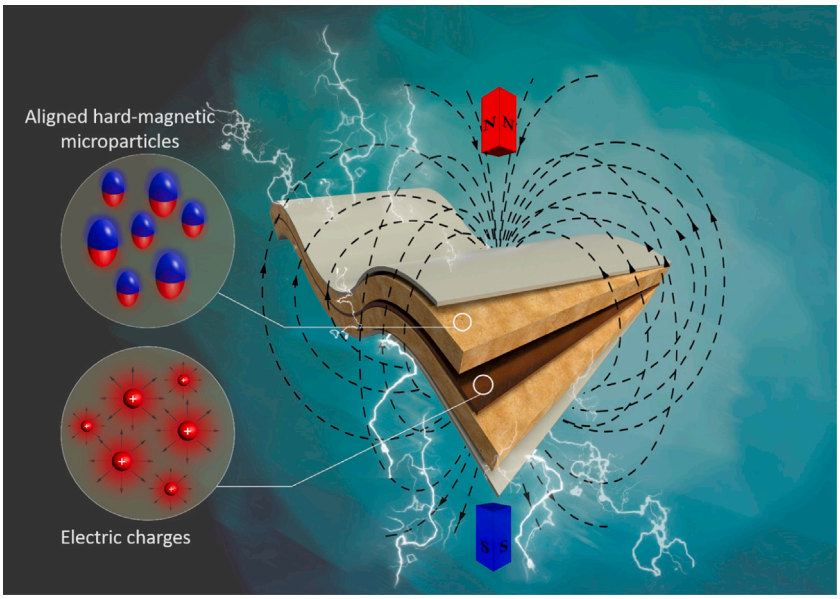

Fig. 1. Schematic of the hard magnetic soft electret material. Applying a magnetic field to a hard magnetic soft electret material can generate an electric field (schematically depicted as lightning) in the material.

2. Theory of hard magnetic soft electrets

In this section, we present a variational approach to derive the governing equations and boundary conditions for hard magnetic soft electret materials. We also justify some of the common approximations that have been used in the past in the context of hard magnetic soft materials c.f. Zhao et al. (2019) and comment on the symmetry of the stress tensor—a notion that appears occasionally to be misinterpreted in the literature.

2.1. Formulation

As will become evident, the emergent magnetoelectric effect requires accounting for nonlinear deformation and accordingly we must distinguish the continuum deformable body in the reference configuration $\Omega_R \subset \mathbb{R}^3$ and current configuration $\Omega \subset \mathbb{R}^3$. As shown in Fig. 2, the deformable body Ω_R is located inside an ambient medium $\mathcal{D}_R$ ($\Omega_R \subset \mathcal{D}_R$) with electric permittivity[3] ϵ_0. The deformation $\chi : \Omega_R \to \Omega$ transforms material points $\mathbf{X}$ in the reference configuration to the spatial points $\mathbf{x}$ in the current configuration. It is assumed that the ambient medium $\mathcal{D}_R$ is elastically trivial with zero elastic stiffness. Thus, the definition of the deformation χ for the points located in $\mathcal{D}_R \setminus \Omega_R$ has no physical meaning and we may choose $\chi \to \mathbf{X}$ quickly away from $\partial\Omega_R$ where $\partial\Omega_R$ denotes the boundary of the body Ω_R. We reserve the symbol ∇ for the gradient in the reference configuration and the differential operators in the current configuration are denoted by "grad" and "div". To define relevant fields in the reference and current configurations, we introduce the deformation gradient $\mathbf{F}$, the Jacobian J, and the right Cauchy–Green strain tensor $\mathbf{C}$:

$$\mathbf{F} = \nabla\chi, \qquad J = \det\mathbf{F} > 0, \qquad \mathbf{C} = \mathbf{F}^T\mathbf{F}.$$

Hard magnetic soft electret materials contain both pre-existing immobile charges or dipoles as well as pre-existing magnetic moments. For electric fields, let $\rho_e : \Omega \to \mathbb{R}$ be the external charge density, $\mathbf{p} : \Omega \to \mathbb{R}^3$ the polarization in the current configuration and $\mathbf{d}$ the electric displacement. For magnetic fields, we assume there are two sources: one is from an external source, i.e., the magnetic field $\mathbf{h}^e = -\mathrm{grad}\phi^e$ in space upon removal of the continuum body, and the pre-existing magnetization due to the embedded hard magnetic particles $\mathbf{m}^r : \Omega \to \mathbb{R}^3$ or residual magnetic flux $\mathbf{b}^r = \mu_0\mathbf{m}^r$ (—μ_0 is the magnetic permeability of vacuum.) Note that the residual magnetic flux is employed in analogy with electric polarization and in general is not divergence-free.

The mechanical, electrostatic and magnetostatic boundary conditions are prescribed as follows. Dirichlet boundary condition $\chi = \chi_b$ are imposed on S_D and tractions $\widetilde{\mathbf{t}}^e$ are applied on S_N ($S_D \cup S_N = \partial\Omega_R$) (Fig. 2). An external voltage $\xi = \xi_b$ may be imposed on Γ_D and $\widetilde{\mathbf{D}} \cdot \mathbf{N} = D_b$ on Γ_N where $\Gamma_D \cup \Gamma_N = \partial\mathcal{D}_R$ and $\mathbf{N}$ denotes unit normal to the boundary in the reference configuration.

[3] We have assumed the ambient medium is vacuum in all the results presented in this paper. However, the formulation presented is general and can be used for any other ambient medium.

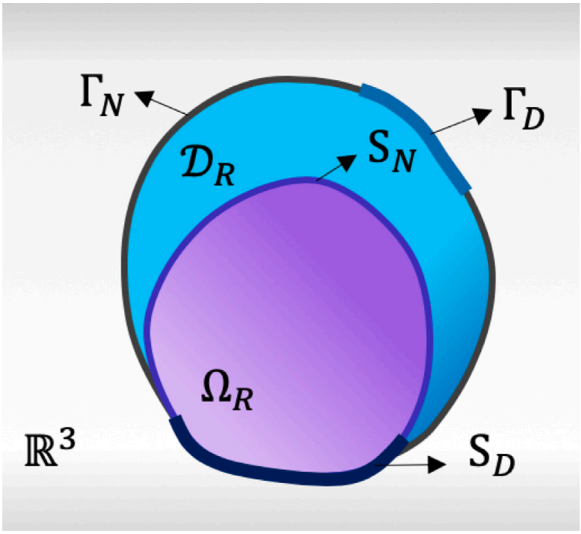

Fig. 2. Continuum deformable body and surrounding medium in the reference configuration.

Neglecting the dynamic coupling between electric and magnetic fields, the Maxwell equations in the current configuration can be written as:

$$\begin{aligned} &\mathbf{e} = -\text{grad}\xi, \qquad \text{div}(\mathbf{d}) = \rho_e, \qquad \mathbf{d} = \epsilon_0\mathbf{e} + \mathbf{p}, \qquad \text{in} \quad \mathcal{D}, \\ &\mathbf{h} = -\text{grad}\phi \qquad \text{div}(\mathbf{b}) = 0, \qquad \mathbf{b} = \mu_0(\mathbf{h} + \mathbf{m}) \qquad \text{in} \quad \mathbb{R}^3. \end{aligned} \tag{1}$$

where $\xi : D \to \mathbb{R}$ (resp. $\phi : \mathbb{R}^3 \to \mathbb{R}$) is the electrostatic (resp. magnetostatic) potential. Note that "resp." is abbreviation for respectively throughout this paper. Further, the total magnetostatic potential can be written as $\phi = \phi^e + \phi^s$, where ϕ^s is due to the magnetization and satisfies

$$\begin{cases} \text{div}\left(\mathbf{h}^s + \mathbf{m}\chi_\Omega\right) = 0 \qquad \text{in} \quad \mathbb{R}^3, \\ |\nabla\phi^s| = O(|\mathbf{x}|^{-3}) \to 0 \qquad \text{as} \quad |\mathbf{x}| \to +\infty, \end{cases} \tag{2}$$

where $\mathbf{h}^s = -\text{grad}\phi^s$ and χ_Ω is the characteristic function of domain Ω satisfying

$$\chi_\Omega = \begin{cases} 1 & \text{on} \quad \Omega, \\ 0 & \text{otherwise}. \end{cases}$$

It will be useful to rewrite the Maxwell equations in Lagrange's coordinates for the reference configuration. To this end, we define[4]

$$\tilde{\mathbf{P}} = J\mathbf{F}^{-1}\mathbf{p}, \qquad \widetilde{\rho}_e = J\rho_e, \qquad \tilde{\mathbf{M}} = J\mathbf{F}^{-1}\mathbf{m}. \tag{3}$$

Upon changes of variables $\mathbf{x} \to \mathbf{X}$, the Maxwell equations in the reference configuration can be written as

$$\begin{aligned} &\nabla \cdot \widetilde{\mathbf{D}} = \widetilde{\rho}_e, \qquad \widetilde{\mathbf{D}} = -\epsilon_0 J\mathbf{C}^{-1}\nabla\xi + \tilde{\mathbf{P}}, \qquad \text{in} \quad D_R, \\ &\nabla \cdot \widetilde{\mathbf{B}} = 0, \qquad \widetilde{\mathbf{B}} = -\mu_0 J\mathbf{C}^{-1}\nabla\phi + \mu_0\tilde{\mathbf{M}}, \qquad \text{in} \quad \mathbb{R}^3. \end{aligned} \tag{4}$$

We remark that the Maxwell Eqs. (4) in the reference configuration, though appear to be "messier" than (1), are convenient for computing the first variation of the free energy and unveiling the origin of the stress associated with electromagnetic fields.

The total free energy of the system that includes the body and boundary loading devices is identified as (Liu, 2014)

$$\mathcal{F}[\chi, \tilde{\mathbf{P}}, \tilde{\mathbf{M}}] = U[\chi, \tilde{\mathbf{P}}, \tilde{\mathbf{M}}] + \mathcal{E}^{\text{elec}}[\chi, \tilde{\mathbf{P}}] + \mathcal{E}^{\text{magnet}}[\chi, \tilde{\mathbf{M}}] - \int_{S_N} \widetilde{\mathbf{t}}^e \cdot \chi, \tag{5}$$

where $U[\chi, \tilde{\mathbf{P}}, \tilde{\mathbf{M}}]$ is the free energy of the body, $\mathcal{E}^{\text{elec}}[\chi, \tilde{\mathbf{P}}]$ (resp. $\mathcal{E}^{\text{magnet}}[\chi, \tilde{\mathbf{M}}]$) is the energy associated with the electric (resp. magnetic field) and boundary devices for maintaining the prescribed boundary conditions. For materials with deformation-independent electric permittivity ϵ and "unmagnetizable" beyond the pre-existing magnetization, we identify the free energy of the

[4] We remark that the polarization $\tilde{\mathbf{P}}$ here is equivalent to $\mathbf{F}^{-1}\tilde{\mathbf{P}}$ in Liu (2014). This change of notation/variables is convenient for prescribing the magnetic constitutive law of the body, separating stresses of different physical origins, and demonstrating the symmetry of the associated Cauchy stress (c.f., Section 2.2).

body $U[\chi, \tilde{\mathbf{P}}, \tilde{\mathbf{M}}]$ as (Liu, 2014)

$$\begin{aligned} U[\chi, \tilde{\mathbf{P}}, \tilde{\mathbf{M}}] &= \int_{\Omega_R} \Psi(\mathbf{F}, \tilde{\mathbf{P}}, \tilde{\mathbf{M}}), \\ \Psi(\mathbf{F}, \tilde{\mathbf{P}}, \tilde{\mathbf{M}}) &= W^{\text{elast}}(\mathbf{F}) + \frac{\tilde{\mathbf{P}} \cdot \mathbf{C}\tilde{\mathbf{P}}}{2J(\epsilon - \epsilon_0)} + \frac{\mu_0^2(\tilde{\mathbf{M}} - \tilde{\mathbf{M}}^r) \cdot \mathbf{C}(\tilde{\mathbf{M}} - \tilde{\mathbf{M}}^r)}{2J(\mu - \mu_0)}, \end{aligned} \tag{6}$$

where the free energy density function $\Psi : \mathbb{R}^{3\times3} \times \mathbb{R}^3 \times \mathbb{R}^3 \to \mathbb{R}$ prescribes the magneto-electro-elastic constitutive behaviors of the material, $\tilde{\mathbf{M}}^r = J\mathbf{F}^{-1}\mathbf{m}^r$ is the pre-existing magnetization due to the hard magnetic particles in the reference configuration, and μ is the linearized magnetic permeability of the body. Contribution of electric field energy $\mathcal{E}^{\text{elec}}$ to the total internal energy is expressed as

$$\mathcal{E}^{\text{elec}}[\chi, \tilde{\mathbf{P}}] = \int_{D_R} \frac{\epsilon_0}{2} J \nabla \xi \cdot \mathbf{C}^{-1} \nabla \xi + \int_{\Gamma_D} \xi_b \mathbf{N} \cdot \tilde{\mathbf{D}}. \tag{7}$$

Similarly, the magnetic contribution $\mathcal{E}^{\text{magnet}}$ is given by

$$\mathcal{E}^{\text{magnet}}[\chi, \tilde{\mathbf{M}}] = \int_{\mathbb{R}^3} \frac{\mu_0}{2} |\mathbf{h}|^2 = \int_{\mathbb{R}^3} \frac{\mu_0}{2} J \nabla\phi \cdot \mathbf{C}^{-1} \nabla\phi. \tag{8}$$

By the principle of minimum free energy, the equilibrium states are determined by minimizing the *total* free energy of the system:

$$\min_{(\chi, \tilde{\mathbf{P}}, \tilde{\mathbf{M}}) \in S} \mathcal{F}[\chi, \tilde{\mathbf{P}}, \tilde{\mathbf{M}}], \tag{9}$$

where admissible space S is defined as

$$S \equiv \{(\chi, \tilde{\mathbf{P}}, \tilde{\mathbf{M}}) \mid \chi = \chi_b \text{ on } S_D,\ \tilde{\mathbf{P}}, \tilde{\mathbf{M}} \text{ are arbitrary}\}. \tag{10}$$

Enforcing the Maxwell's Eqs. (4) as constraints, we use the standard variational process to derive the governing Euler–Lagrange equations associated with the variational principle (9). We omit details of derivation here since the procedure is standard and key elements may be found in, e.g., Liu (2014). In particular, we find the relevant first-variations as follows:

$$\begin{aligned} \frac{d}{d\varepsilon}\Big|_{\varepsilon=0} \mathcal{F}[\chi + \varepsilon\chi_1, \tilde{\mathbf{P}}, \tilde{\mathbf{M}}] &= \int_{\Omega_R} \widetilde{\boldsymbol{\Sigma}}^{\text{tot}} \cdot \nabla \chi_1, \\ \frac{d}{d\varepsilon}\Big|_{\varepsilon=0} \mathcal{F}[\chi, \tilde{\mathbf{P}} + \varepsilon\tilde{\mathbf{P}}_1, \tilde{\mathbf{M}}] &= \int_{\Omega_R} (\frac{\partial \Psi}{\partial \tilde{\mathbf{P}}} + \nabla\xi) \cdot \tilde{\mathbf{P}}_1, \\ \frac{d}{d\varepsilon}\Big|_{\varepsilon=0} \mathcal{F}[\chi, \tilde{\mathbf{P}}, \tilde{\mathbf{M}} + \varepsilon\tilde{\mathbf{M}}_1] &= \int_{\Omega_R} (\frac{\partial \Psi}{\partial \tilde{\mathbf{M}}} + \mu_0 \nabla\phi) \cdot \tilde{\mathbf{M}}_1, \end{aligned} \tag{11}$$

where $\chi_1 : \Omega_R \to \mathbb{R}^3$ is any displacement satisfying $\chi_1 = 0$ on $\partial\Omega_R$, and

$$\begin{aligned} \widetilde{\boldsymbol{\Sigma}}^{\text{tot}} &= \chi_{\Omega_R}\Big(\widetilde{\boldsymbol{\Sigma}} + \widetilde{\boldsymbol{\Sigma}}^{\text{MW}}_{\text{elec}} + \widetilde{\boldsymbol{\Sigma}}^{\text{MW}}_{\text{magnet}}\Big), \qquad \widetilde{\boldsymbol{\Sigma}} = \frac{\partial \Psi(\mathbf{F}, \tilde{\mathbf{P}}, \tilde{\mathbf{M}})}{\partial \mathbf{F}}, \\ \widetilde{\boldsymbol{\Sigma}}^{\text{MW}}_{\text{elec}} &= -\frac{\epsilon_0}{2} J |\mathbf{F}^{-T} \nabla\xi|^2 \mathbf{F}^{-T} - \mathbf{F}^{-T} \nabla\xi \otimes (-\epsilon_0 J \mathbf{C}^{-1} \nabla\xi), \\ \widetilde{\boldsymbol{\Sigma}}^{\text{MW}}_{\text{magnet}} &= -\frac{\mu_0}{2} J |\mathbf{F}^{-T} \nabla\phi|^2 \mathbf{F}^{-T} - \mathbf{F}^{-T} \nabla\phi \otimes (-\mu_0 J \mathbf{C}^{-1} \nabla\phi). \end{aligned} \tag{12}$$

From (11) we identify the physical meaning of $\widetilde{\boldsymbol{\Sigma}}^{\text{tot}}$ as the total Piola–Kirchhoff stress. Consequently, the Euler–Lagrange equations for equilibrium states read

$$\begin{aligned} &\nabla \cdot \Big(\widetilde{\boldsymbol{\Sigma}} + \widetilde{\boldsymbol{\Sigma}}^{\text{MW}}_{\text{elec}} + \widetilde{\boldsymbol{\Sigma}}^{\text{MW}}_{\text{magnet}}\Big) = 0 && \text{in} \quad \Omega_R, \\ &\mathbf{F}^{-T} \nabla\xi + \frac{\mathbf{F}\tilde{\mathbf{P}}}{J(\epsilon - \epsilon_0)} = 0 && \text{in} \quad \Omega_R, \\ &\mathbf{F}^{-T} \nabla\phi + \frac{\mu_0 \mathbf{F}(\tilde{\mathbf{M}} - \tilde{\mathbf{M}}^r)}{J(\mu - \mu_0)} = 0 && \text{in} \quad \Omega_R. \end{aligned} \tag{13}$$

In particular, in the current configuration the last two of the above equations are equivalent to

$$\mathbf{e} = \frac{\mathbf{p}}{\epsilon - \epsilon_0}, \qquad \mathbf{h} = \frac{\mathbf{m} - \mathbf{m}^r}{\mu/\mu_0 - 1}.$$

As $\mu \to \mu_0$, the last equation implies

$$\mathbf{m} \to \mathbf{m}^r, \qquad \mathbf{b} = \mu_0(\mathbf{h} + \mathbf{m}) = \mu\mathbf{h} + \mu_0\mathbf{m}^r \to \mu_0(\mathbf{h} + \mathbf{m}^r),$$

meaning that the body is hardly magnetizable beyond the pre-existing magnetization $\mathbf{m}^r$. In other words, the magnetization on each material point is given by $\tilde{\mathbf{M}}^r$ in the reference configuration that will be independent of the deformation and externally applied magnetic field. Subsequently, we assume

$$\mu = \mu_0.$$

In addition, on the boundary S_N, a quick free-body diagram analysis (or a more careful calculus of variations for general χ_1 that is nonzero on S_N) yields

$$[\![\widetilde{\boldsymbol{\Sigma}} + \widetilde{\boldsymbol{\Sigma}}^{\mathrm{MW}}_{\mathrm{elec}} + \widetilde{\boldsymbol{\Sigma}}^{\mathrm{MW}}_{\mathrm{magnet}}]\!] \cdot \mathbf{N} + \widetilde{\mathbf{t}}^{e} = \mathbf{0} \qquad \text{on} \quad S_N, \tag{14}$$

where $[\![(\cdot)]\!] = (\cdot)_+ - (\cdot)_-$ represents the jump across the interface, and subscript $_+$ (resp. $_-$) means the interface side pointed by $\mathbf{N}$ (resp. $-\mathbf{N}$).

Due to the particular form of free energy density (6) and the symmetry and symmetry broken by the external magnetic field, it is physically more transparent to transform the Piola–Kirchhoff stresses into Cauchy stress via

$$\boldsymbol{\Sigma} \to \boldsymbol{\sigma} = \frac{1}{J}\boldsymbol{\Sigma}\mathbf{F}^T, \tag{15}$$

and combine or decompose stresses in (12) as follows. First, we notice that

$$\begin{aligned}
&\frac{\partial}{\partial \mathbf{F}}\Big(\frac{\tilde{\mathbf{P}}\cdot\mathbf{C}\tilde{\mathbf{P}}}{2J(\epsilon-\epsilon_0)}\Big) = \frac{(\mathbf{F}\tilde{\mathbf{P}})\otimes\tilde{\mathbf{P}}}{J(\epsilon-\epsilon_0)} - \frac{|\mathbf{F}\tilde{\mathbf{P}}|^2}{J(\epsilon-\epsilon_0)}\mathbf{F}^{-T} \to \frac{1}{\epsilon-\epsilon_0}\big[\mathbf{p}\otimes\mathbf{p} - |\mathbf{p}|^2\frac{\mathbf{I}}{2}\big],\\
&\frac{\partial}{\partial \mathbf{F}}\Big(\frac{\mu_0^2(\tilde{\mathbf{M}}-\tilde{\mathbf{M}}^r)\cdot\mathbf{C}(\tilde{\mathbf{M}}-\tilde{\mathbf{M}}^r)}{2J(\mu-\mu_0)}\Big) \to \frac{\mu_0^2}{\mu-\mu_0}\big[(\mathbf{m}-\mathbf{m}^r)\otimes(\mathbf{m}-\mathbf{m}^r) - |\mathbf{m}-\mathbf{m}^r|^2\frac{\mathbf{I}}{2}\big].
\end{aligned}$$

Singling out the elastic contribution and merging the rest to electromagnetic Maxwell stresses we obtain

$$\frac{1}{J}(\widetilde{\boldsymbol{\Sigma}} + \widetilde{\boldsymbol{\Sigma}}^{\mathrm{MW}}_{\mathrm{elec}} + \widetilde{\boldsymbol{\Sigma}}^{\mathrm{MW}}_{\mathrm{magnet}})\mathbf{F}^T = \boldsymbol{\sigma}^{\mathrm{elast}} + \boldsymbol{\sigma}^{\mathrm{MW}}_{\mathrm{elec}} + \boldsymbol{\sigma}^{\mathrm{MW}}_{\mathrm{magnet}} \qquad \text{in} \quad \Omega, \tag{16}$$

where

$$\begin{aligned}
&\boldsymbol{\sigma}^{\mathrm{elast}} = \frac{\partial W^{\mathrm{elast}}(\mathbf{F})}{J\partial\mathbf{F}}\mathbf{F}^T, \qquad \boldsymbol{\sigma}^{\mathrm{MW}}_{\mathrm{elec}} = -\frac{\epsilon}{2}|\mathbf{e}|^2\mathbf{I} + \mathbf{e}\otimes(\epsilon\mathbf{e}),\\
&\boldsymbol{\sigma}^{\mathrm{MW}}_{\mathrm{magnet}} = -\frac{\mu_0}{2}|\mathbf{h}|^2\mathbf{I} + \mathbf{h}\otimes(\mu_0\mathbf{h}).
\end{aligned} \tag{17}$$

Second, separating the contributions of external magnetic field and pre-existing magnetization, we rewrite the magnetic Maxwell stress as

$$\boldsymbol{\sigma}^{\mathrm{MW}}_{\mathrm{magnet}} = \boldsymbol{\sigma}^{e}_{\mathrm{magnet}} + \boldsymbol{\sigma}^{s}_{\mathrm{magnet}} + \boldsymbol{\sigma}^{\mathrm{int}}_{\mathrm{magnet}},$$

where the superscript ^{e} (resp. ^{s}, $^{\mathrm{int}}$) means "external" (resp. "self", "interaction"). That is,

$$\begin{aligned}
&\boldsymbol{\sigma}^{e}_{\mathrm{magnet}} = \mu_0\mathbf{h}^e\otimes\mathbf{h}^e - \frac{\mu_0}{2}|\mathbf{h}^e|^2\mathbf{I}, \qquad \boldsymbol{\sigma}^{s}_{\mathrm{magnet}} = \mu_0\mathbf{h}^s\otimes\mathbf{h}^s - \frac{\mu_0}{2}|\mathbf{h}^s|^2\mathbf{I},\\
&\boldsymbol{\sigma}^{\mathrm{int}}_{\mathrm{magnet}} = \mu_0\mathbf{h}^s\otimes\mathbf{h}^e + \mu_0\mathbf{h}^e\otimes\mathbf{h}^s - \mu_0(\mathbf{h}^e\cdot\mathbf{h}^s)\mathbf{I}.
\end{aligned} \tag{18}$$

Recall that $\mathbf{h}^e = -\nabla\phi^e$ is the externally applied magnetic field and satisfies $\mathrm{div}(\mathbf{h}^e) = \phi^e_{,kk} = 0$ on $\mathbb{R}^3$ and $\mathbf{h}^s = -\nabla\phi^s$ is the self magnetic field arising from the preexisting magnetization. Therefore,

$$\begin{aligned}
(\boldsymbol{\sigma}^{e}_{\mathrm{magnet}})_{ij,j} &= \mu_0\phi^e_{,ij}\phi^e_{,j} + \mu_0\phi^e_{,i}\phi^e_{,jj} - \mu_0\phi^e_{,ki}\phi^e_{,k} = 0,\\
(\boldsymbol{\sigma}^{s}_{\mathrm{magnet}})_{ij,j} &= \mu_0\phi^s_{,ij}\phi^s_{,j} + \mu_0\phi^s_{,i}\phi^s_{,jj} - \mu_0\phi_{,ki}\phi^s_{,k} = \mu_0\phi^s_{,i}\phi^s_{,jj},\\
(\boldsymbol{\sigma}^{\mathrm{int}}_{\mathrm{magnet}})_{ij,j} &= \mu_0\phi^s_{,ij}\phi^e_{,j} + \mu_0\phi^s_{,i}\phi^e_{,jj} + \mu_0\phi^e_{,ij}\phi^s_{,j} + \mu_0\phi^e_{,i}\phi^s_{,jj} - \mu_0\phi^e_{,ki}\phi^s_{,k} - \mu_0\phi^e_{,k}\phi^s_{,ki}\\
&= \mu_0\phi^e_{,i}\phi^s_{,jj}.
\end{aligned}$$

In direct notation, the results of the above calculations can be concisely written as $\mathrm{div}\boldsymbol{\sigma}^{e}_{\mathrm{magnet}} = 0$ in $\mathbb{R}^3$, and

$$\begin{aligned}
&\mathrm{div}\boldsymbol{\sigma}^{s}_{\mathrm{magnet}} = \mu_0\mathbf{h}^s\mathrm{div}\mathbf{h}^s = -\mu_0\mathbf{h}^s\mathrm{div}(\mathbf{m}^r\chi_\Omega) \qquad \text{in} \quad \mathbb{R}^3,\\
&\mathrm{div}\boldsymbol{\sigma}^{\mathrm{int}}_{\mathrm{magnet}} = \mu_0\mathbf{h}^e\mathrm{div}\mathbf{h}^s = -\mu_0\mathbf{h}^e\mathrm{div}(\mathbf{m}^r\chi_\Omega) \qquad \text{in} \quad \mathbb{R}^3,
\end{aligned} \tag{19}$$

where the last equality follows from (2).

A few remarks are in order here regarding the definition and mechanical effects of the "Maxwell stress". First of all, there is no consensus on the definition of Maxwell stress in the literature. This issue arises from the different way of decomposing the total free energy into the elastic part and electromagnetic part (Toupin, 1960), and the choice is often for the convenience of a particular material model. For instance, the Maxwell stress on the right hand side of (16) is not the same as on the left hand side, besides the transformation (15). In other words, the precise expression of Maxwell stress depends on the material model and how the total stress is decomposed into the elastic part and electromagnetic part. Second, from the fundamental physics it is indisputable that the force on a *point* magnetic moment $\mathbf{m} \in \mathbb{R}^3$ in an external field $\mathbf{h}^e$ is given by $\mu_0(\nabla\mathbf{h}^e)\mathbf{m}$ (Jackson, 1999). Now we consider a continuum body Ω with magnetization $\mathbf{m} : \Omega \to \mathbb{R}^3$, the total magnetic body force on the body should be given by

$$\mathbf{f}_{\mathrm{magnet}} \equiv \int_\Omega \mu_0(\nabla\mathbf{h})\mathbf{m} = \int_\Omega \mu_0(\nabla\mathbf{h}^e)\mathbf{m}, \tag{20}$$

provided the total magnetic field $\mathbf{h} = -(\nabla\phi^e + \nabla\phi^s)$ is differentiable. Indeed, suppose the magnetization $\mathbf{m} : \Omega \to \mathbb{R}^3$ is continuous and vanishes on $\partial\Omega$, implying the magnetic field $\mathbf{h}$ is continuously differentiable on $\mathbb{R}^3$. By (19) we have

$$\begin{aligned}\int_\Omega \mathrm{div}\boldsymbol{\sigma}_{\mathrm{magnet}} &= \int_\Omega \left[\mathrm{div}(\boldsymbol{\sigma}^e_{\mathrm{magnet}} + \boldsymbol{\sigma}^s_{\mathrm{magnet}} + \boldsymbol{\sigma}^{\mathrm{int}}_{\mathrm{magnet}})\right]\\ &= \int_\Omega \mathrm{div}(\boldsymbol{\sigma}^s_{\mathrm{magnet}}) - \mu_0\int_\Omega \mathbf{h}^e\mathrm{div}(\mathbf{m}) = -\mu_0\int_\Omega \left[\mathrm{div}(\mathbf{h}^e\otimes\mathbf{m}) - (\nabla\mathbf{h}^e)\mathbf{m}\right]\\ &= \mu_0\int_\Omega (\nabla\mathbf{h}^e)\mathbf{m},\end{aligned}$$

which is consistent with (20). Here, we have used (B_R is the radius-R ball centered at the origin)

$$\int_\Omega \mathrm{div}(\boldsymbol{\sigma}^s_{\mathrm{magnet}}) = \lim_{R\to+\infty}\int_{B_R}\mathrm{div}(\boldsymbol{\sigma}^s_{\mathrm{magnet}}) = \lim_{R\to+\infty}\int_{\partial B_R}\boldsymbol{\sigma}^s_{\mathrm{magnet}}\mathbf{n}da \to 0. \tag{21}$$

Physically, the above equation (21) means that the total magnetic force on the magnetic body due to its own magnetization should vanish (as implied by the Newton's Third Law), though the local stress due to magnetic interaction is in general nonzero. Finally, we emphasize that the integrand of (20), i.e., $\mu_0(\nabla\mathbf{h}^e)\mathbf{m}$ or $\mu_0(\nabla\mathbf{h})\mathbf{m}$ in general cannot be interpreted as the body force due to magnetization in the continuum body.[5]

To summarize, by (1), (2), and (13) the field equations in the current configuration for determining the magneto-electro-elastic equilibrium states consist of

$$\begin{aligned}&\mathrm{div}\left(\boldsymbol{\sigma}^{\mathrm{elast}} + \boldsymbol{\sigma}^{\mathrm{MW}}_{\mathrm{elec}} + \boldsymbol{\sigma}^s_{\mathrm{magnet}}\right) = -\mathrm{div}(\boldsymbol{\sigma}^{\mathrm{int}}_{\mathrm{magnet}}) && \text{in}\quad \Omega,\\ &\mathrm{div}(-\nabla\phi^s + \mathbf{m}^r\chi_\Omega) = 0 && \text{in}\quad \mathbb{R}^3,\\ &\mathrm{div}(-\varepsilon\nabla\xi) = \rho_e && \text{in}\quad D,\end{aligned} \tag{22}$$

where the Maxwell stresses are given by (17) and (18). We can see that (22) represents a coupled nonlinear system for deformation-magnetostatic potential and electric potential (χ, ϕ^s, ξ).

A technical difficulty in solving (22) lies in the necessity of solving the magnetostatic equation (2) for the nonlocal self magnetic field $\mathbf{h}^s = -\nabla\phi^s$. From $(19)_2$, we see that the body force contributed by $\boldsymbol{\sigma}^{\mathrm{int}}_{\mathrm{magnet}}$ depends only on the external field $\mathbf{h}^e$ and pre-existing magnetization $\mathbf{m}^r$. In particular, if the external magnetic field $\mathbf{h}^e$ is uniform, we have

$$\mathrm{div}\boldsymbol{\sigma}^{\mathrm{int}}_{\mathrm{magnet}} = -\mu_0\mathrm{div}\left(\mathbf{h}^e\otimes\mathbf{m}^r\chi_\Omega\right). \tag{23}$$

The self magnetic Maxwell stress $\boldsymbol{\sigma}^s_{\mathrm{magnet}}$ does depend on the self-magnetic field and, quantitatively, could be non-negligible as compared with $\boldsymbol{\sigma}^{\mathrm{int}}$ since the pre-existing magnetization $\mathbf{m}^r$ may be large for hard-magnetic particles. Nevertheless, we notice that the body forces contributed by $\boldsymbol{\sigma}^s_{\mathrm{magnet}}$ form a self-equilibrated force system in the sense that the resultant force on the body vanishes (c.f., (21)) and the resultant torque on the body also vanishes:

$$\begin{aligned}\int_\Omega [\mathbf{x}\times\mathrm{div}(\boldsymbol{\sigma}^s_{\mathrm{magnet}})]_i &= \lim_{R\to+\infty}\int_{B_R}\{[\mathcal{E}_{ijk}x_j(\boldsymbol{\sigma}^s_{\mathrm{magnet}})_{kl}]_{,l} - [\mathcal{E}_{ijk}\delta_{jl}(\boldsymbol{\sigma}^s_{\mathrm{magnet}})_{kl}]\}\\ &= \lim_{R\to+\infty}\int_{\partial B_R}\mathcal{E}_{ijk}x_j(\boldsymbol{\sigma}^s_{\mathrm{magnet}})_{kl}n_l da \to 0,\end{aligned} \tag{24}$$

where $\mathcal{E}_{ijk}$ (resp. δ_{ij}) is the Levi-Civita symbol (resp. Kronecker delta) and the last step follows from $(2)_2$. Therefore, the self magnetic Maxwell stress, as the conventional residual stress, may be taken into account by choosing the reference configuration as the initial configuration (instead of the "stress-free" configuration) of the body before applying any external forces or electromagnetic fields. From this viewpoint, we can neglect the self-magnetic Maxwell stress and rewrite $(22)_1$ as[6]

$$\mathrm{div}\left(\boldsymbol{\sigma}^{\mathrm{elast}} + \boldsymbol{\sigma}^{\mathrm{MW}}_{\mathrm{elec}}\right) = -\mathrm{div}(\boldsymbol{\sigma}^{\mathrm{int}}_{\mathrm{magnet}}) = \mu_0\mathbf{h}^e\mathrm{div}(\mathbf{m}^r\chi_\Omega) \qquad \text{in}\quad \Omega, \tag{25}$$

which makes solution to the magnetostatic equation$(22)_2$ unnecessary. In other words, the magnetic Piola–Kirchhoff Maxwell stress in the mechanical balance equation $(13)_1$ could be replaced by

$$\tilde{\boldsymbol{\Sigma}}^{\mathrm{MW}}_{\mathrm{magnet}} \approx -\mu_0\mathbf{h}^e\otimes\tilde{\mathbf{M}}^r \tag{26}$$

if the external magnetic field $\mathbf{h}^e$ is uniform. In the illustrative examples presented in later sections, we will employ the simplified stress terms (26) for our calculations. We remark that the preceding paragraph justifies the approximate relation (26) used in the prior work of some of the authors (Zhao et al., 2019).

[5] This appears to be a common misconception in the literature on deformable continuum magneto-electro-elasticity. With this said, our ensuring discussion also provides justification for why some of the common approximations work well

[6] For small deformation and linearized elasticity, this change of reference configuration suffices for predicting elastic fields induced by external loadings without any error. For large deformation and nonlinear elasticity, this approach is an approximation to address the effects of a self-equilibrated force system which, in our experience, appears to be very good.

2.2. Symmetry of the Cauchy stress

A frequent contention is that in the context of magnetism "stress" is asymmetric. Usually, such statements emerge due to the difference in how the so-called "stress" is identified—see for example the prior work of some of the authors (Zhao et al., 2019). Suppose the total free energy $F[\chi, \tilde{\mathbf{P}}, \tilde{\mathbf{M}}]$ of the system admits the following properties:

1. *Locality*.[7] The functional derivative of the free energy with respect to deformation can be written as
$$\frac{d}{d\varepsilon}\Big|_{\varepsilon=0} F[\chi + \varepsilon\chi_1, \tilde{\mathbf{P}}, \tilde{\mathbf{M}}] = \int_{\Omega_R} \boldsymbol{\Sigma} \cdot \nabla\chi_1 d\mathbf{X} = \int_{\Omega} \frac{1}{J}\boldsymbol{\Sigma}\mathbf{F}^T \cdot \mathrm{grad}\chi_1 d\mathbf{x}, \tag{27}$$
where $\boldsymbol{\Sigma}$ (resp. $\boldsymbol{\sigma} = \boldsymbol{\Sigma}\mathbf{F}^T/J$) is identified as the *total* Piola–Kirchhoff stress (resp. the total Cauchy stress).
2. *Frame-indifference*. Let $\mathbf{Q}(s) = \exp(s\mathbf{W})$ be rigid rotations parametrized by s and an arbitrary skew-symmetric matrix $\mathbf{W} \in \mathbb{R}^{3\times3}$. The free energy is invariant under a superimposed rigid rotation:
$$F[\mathbf{Q}(s)\chi, \tilde{\mathbf{P}}, \tilde{\mathbf{M}}] = F[\chi, \tilde{\mathbf{P}}, \tilde{\mathbf{M}}].$$
By (27), the frame-indifference implies that for any skew-symmetric matrix $\mathbf{W} \in \mathbb{R}^{3\times3}$,
$$\begin{aligned} 0 \equiv \frac{d}{ds}\Big|_{s=0} F[\mathbf{Q}(s)\chi, \tilde{\mathbf{P}}, \tilde{\mathbf{M}}] &= \frac{d}{ds}\Big|_{s=0} F[\chi + s\mathbf{W}\chi, \tilde{\mathbf{P}}, \tilde{\mathbf{M}}] \\ &= \int_{\Omega_R} \boldsymbol{\Sigma} \cdot \nabla(\mathbf{W}\chi(\mathbf{X}))d\mathbf{X} = \int_{\Omega} \frac{1}{J}\boldsymbol{\Sigma}\mathbf{F}^T \cdot \mathbf{W} d\mathbf{x}. \end{aligned}$$
Therefore, the Cauchy stress
$$\boldsymbol{\sigma} := \frac{1}{J}\boldsymbol{\Sigma}\mathbf{F}^T$$
must be symmetric if the free energy is invariant with respect to superimposed rigid rotations.

We remark that the total free energy for the system defined by (5), strictly speaking, is neither local (in the sense of (27)) nor frame-indifferent because of the applied mechanical boundary condition (the last term of (5)). However, the energy functional at the absence of applied mechanical traction
$$F[\chi, \tilde{\mathbf{P}}, \tilde{\mathbf{M}}] = U[\chi, \tilde{\mathbf{P}}, \tilde{\mathbf{M}}] + \mathcal{E}^{\mathrm{elec}}[\chi, \tilde{\mathbf{P}}] + \mathcal{E}^{\mathrm{magnet}}[\chi, \tilde{\mathbf{M}}]$$
is indeed local and frame-indifferent. By $(11)_1$, (12), and (16), we conclude that the *total* Cauchy stress
$$\boldsymbol{\sigma}^{\mathrm{tot}} := \frac{1}{J}\tilde{\boldsymbol{\Sigma}}^{\mathrm{tot}}\mathbf{F}^T = \boldsymbol{\sigma}^{\mathrm{elast}} + \boldsymbol{\sigma}^{\mathrm{MW}}_{\mathrm{elec}} + \boldsymbol{\sigma}^{s}_{\mathrm{magnet}}$$
must be symmetric.

Physically, it is only the divergence of an electromagnetic Maxwell stress that matters for the mechanical balance. Therefore, it is sometimes convenient to rewrite a complicated symmetric Maxwell stress in a simpler non-symmetric form with the same divergence, e.g., $\boldsymbol{\sigma}^{\mathrm{int}}_{\mathrm{magnet}} \to -\mu_0\mathbf{h}^e \otimes \mathbf{m}^r$ as in (23).

3. Numerical solution procedure for incompressible materials

The equations in the preceding section can only be solved analytically for simple geometries. To handle non-trivial boundary value problems we have developed a finite element solution for the our framework. There are several implementations for similar coupled problems available in the literature (Henann et al., 2013; Zhao and Suo, 2008; Zhao et al., 2019). We use an approach which enables numerical solutions without using any commercial packages. Our computational procedure for incompressible materials, with minor modifications, can be used for compressible materials as well. The weak form of the Eqs. (4) and (13) are given as
$$\int_{D_R} \nabla w_1 \cdot \tilde{\mathbf{D}} + \int_{D_R} w_1\tilde{\rho}_e = 0, \tag{28}$$
$$\int_{\mathbb{R}^3} \nabla w_2 \cdot \tilde{\mathbf{B}} = 0, \tag{29}$$
$$\int_{\mathbb{R}^3} \nabla \mathbf{w}_3 \cdot \tilde{\boldsymbol{\Sigma}}^{\mathrm{tot}} \chi_{\Omega_R} = \mathbf{0} \tag{30}$$
$$\int_{\Omega_R} \left[w_4\,(\det\mathbf{F} - 1)\right] = 0, \tag{31}$$
where $(w_1, w_2, \mathbf{w}_3, w_4) \in \mathcal{W}$ and
$$\mathcal{W} \equiv \{(w_1, w_2, \mathbf{w}_3, w_4)\Big| w_1 = 0 \quad \text{on} \quad \Gamma_D, \quad \mathbf{w}_3 = 0 \quad \text{on} \quad S_D\}. \tag{32}$$

[7] The locality usually refers to the Lagrangian as a local function of the fields. Here, we focus on the functional derivative of free energy with respect to the strain field and the property of locality (27) is slightly more general.

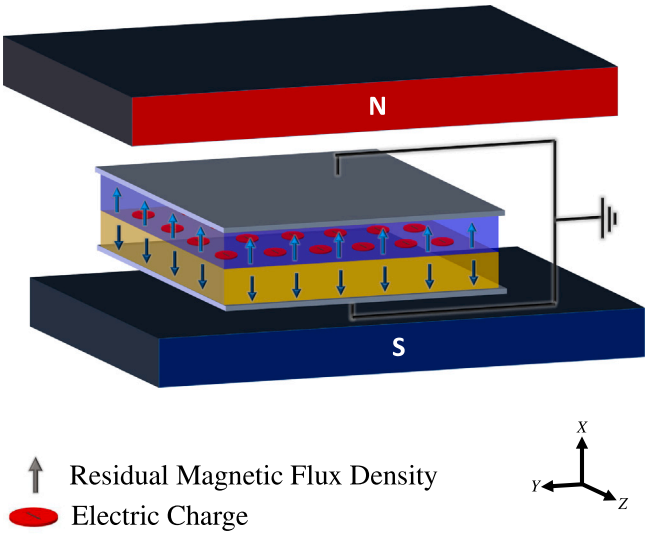

Fig. 3. The schematic of bilayer HMSE made of two layers with different material properties.

The hydrostatic pressure $\mathcal{L}_a$ is a Lagrange multiplier which has been introduced to enforce the incompressibility constraint to avoid numerical oscillations and volumetric locking. We make use of Taylor–Hood elements which implies that the order of shape functions used for the discretization of displacement is one order higher than the that for the pressure. The Taylor–Hood elements have been successfully used in various problems (Chen et al., 2020; Garcia-Gonzalez and Landis, 2020). It can be proved that Taylor–Hood elements satisfy the Ladyzhenskaya–Babuska–Brezzi (LBB) condition which is required for the stability of mixed method in incompressible elasticity and Stokes flow (Babuška, 1971; Brezzi, 1974; Fortin and Brezzi, 1991; Bouklas et al., 2015). Therefore, we use quadratic interpolation for displacement and linear shape function for electric potential, magnetic potential and hydrostatic pressure. The actual solution of the equations is through the open-source solver FEniCS (Logg et al., 2012).

4. Illustrative analytical examples

4.1. Magnetoelectricity under tension or compression

Consider the hard magnetic soft electret configuration shown in Fig. 3. This electret consists of two different materials on top and bottom which are referenced with subscripts $_t$ and $_b$, respectively. Let $\mathbf{X} = X\mathbf{e}_X + Y\mathbf{e}_Y + Z\mathbf{e}_Z$ be the representation of the points in the Lagrange coordinates while points in the Euler coordinates are denoted by $\mathbf{x} = x\mathbf{e}_x + y\mathbf{e}_y + z\mathbf{e}_z$. The top layer has thickness H_t and thickness of bottom layer is denoted by H_b. There is a layer of charge between two layers with surface charge density q_0. The material is sandwiched between two mechanically compliant electrodes on top and bottom and short circuit boundary condition is imposed. There is uniform residual magnetic flux density $\widetilde{\mathbf{B}}^r = \mu_0\mathbf{M}^r = B_t^r\mathbf{e}_X$ (resp. $\widetilde{\mathbf{B}}^r = B_b^r\mathbf{e}_X$) in top (resp. bottom) layer. The material will deform in response to an externally applied magnetic flux density $\mathbf{b}^{\text{app}} = b^{\text{app}}\mathbf{e}_x = \mu_0\mathbf{h}^e$. Since the two layers have different material properties, deformation in two layers will not be the same.[8]

Let the deformation gradient tensor for each layer be expressed as

$$\mathbf{F} = \lambda_t\mathbf{e}_x \otimes \mathbf{e}_X + \lambda_t^{-1/2}\mathbf{e}_y \otimes \mathbf{e}_Y + \lambda_t^{-1/2}\mathbf{e}_z \otimes \mathbf{e}_Z \qquad \text{for} \quad H_b < X < H_b + H_t \tag{33}$$

$$\mathbf{F} = \lambda_b\mathbf{e}_x \otimes \mathbf{e}_X + \lambda_b^{-1/2}\mathbf{e}_y \otimes \mathbf{e}_Y + \lambda_b^{-1/2}\mathbf{e}_z \otimes \mathbf{e}_Z \qquad \text{for} \quad 0 < X < H_b \tag{34}$$

Considering uniform deformation, thickness of each layer in the deformed configuration may be determined to be:

$$h_t = \lambda_t H_t, \tag{35}$$

$$h_b = \lambda_b H_b. \tag{36}$$

Moreover, considering short circuit boundary condition and assuming uniform electric field in both top and bottom layers, electric fields can be derived to be

$$\mathbf{e} = -\frac{\mathrm{d}\xi}{\mathrm{d}x} = \begin{cases} \frac{V}{h_t} & \text{for} \quad h_b < X < h_b + h_t, \\ -\frac{V}{h_b} & \text{for} \quad 0 < X < h_b, \end{cases} \tag{37}$$

[8] It is important to note that unequal deformation in the two layers may lead to the bending. However, for this simplified example, we ignore this contribution

where, using Maxwell's equations, V is determined from the following equation

$$\epsilon_t \frac{V}{h_t} + \epsilon_b \frac{V}{h_b} = q_0. \tag{38}$$

We use the incompressible neo-Hookean constitutive relation:

$$W^{elast}[\mathbf{F}] = \frac{G_i}{2}(\mathrm{tr}(\mathbf{F}^T\mathbf{F}) - 3), \qquad \text{for} \quad i = t, b \tag{39}$$

where G denotes the shear modulus of the material. Assuming constant external magnetic field and using simplified form of the magnetic Maxwell stress, the equilibrium equations for each layer reduces to

$$(\lambda_t^2 - \frac{1}{\lambda_t}) - \lambda_t \bar{B}_t + \frac{\epsilon_t}{G_t}\left(\frac{V}{h_t}\right)^2 = 0, \tag{40}$$

$$(\lambda_b^2 - \frac{1}{\lambda_b}) - \lambda_b \bar{B}_b + \frac{\epsilon_b}{G_b}\left(\frac{V}{h_b}\right)^2 = 0. \tag{41}$$

where $\bar{B} = \mu_0^{-1} G^{-1} \widetilde{\mathbf{B}}^r \cdot \mathbf{b}^{\mathrm{app}}$ and $\bar{B}_t$ and $\bar{B}_b$ are the corresponding values of $\bar{B}$ in top and bottom layers, respectively. We can then analytically determine the linearized solution for the above equations assuming $|\lambda_b - 1| \ll 1$ and $|\lambda_t - 1| \ll 1$:

$$\lambda_t \approx \frac{1}{1 - \bar{B}_t/3} - \frac{\epsilon_t/3G_t}{1 - \bar{B}_t/3}\left(\frac{H_b q_0}{H_t\epsilon_b + H_b\epsilon_t}\right)^2, \tag{42}$$

$$\lambda_b \approx \frac{1}{1 - \bar{B}_b/3} - \frac{\epsilon_b/3G_b}{1 - \bar{B}_b/3}\left(\frac{H_t q_0}{H_b\epsilon_t + H_t\epsilon_b}\right)^2. \tag{43}$$

Unless an external electric field is applied to the material, the magnitude of electric Maxwell stress is often negligible. Ignoring the effect of electric Maxwell stress in Eqs. (42) and (43), we can rewrite the last two equations as

$$\lambda_t - 1 \approx \frac{B_t^r b_t^{\mathrm{app}}}{3\mu_0 G_t}, \tag{44}$$

$$\lambda_b - 1 \approx \frac{B_b^r b_b^{\mathrm{app}}}{3\mu_0 G_b}. \tag{45}$$

With the stretches in each layer at hand, we can determine both the electric field and electric displacement. Electric displacement in top layer is expressed as $\widetilde{\mathbf{D}} = D_t \mathbf{e}_X$ where D_t is determined by substituting Eq. (38) into Eq. (37):

$$D_t \approx D^i + \frac{q H_t H_b \epsilon_b \epsilon_t (\lambda_b - \lambda_t)}{(H_t\epsilon_b + H_b\epsilon_t)^2}, \tag{46}$$

where D^i is the deformation independent part of the electric displacement. For brevity and ease in presentation of equation, we have assumed $\mathbf{d} \approx \widetilde{\mathbf{D}}$ in derivation of Eq. (46).

For conventional magnetostrictive/piezoelectric composites, magnetoelectric coupling coefficient is defined as (Nan et al., 2008; Fiebig, 2005)

$$\alpha_{ij} = \frac{\partial P_i}{\partial h_j^e}, \tag{47}$$

where h_i^e and P_j, respectively, are the components of the magnetic field and electric polarization defined in a linear framework where there is no difference between reference and current configurations. Also, magnetoelectric voltage coefficient $\boldsymbol{\alpha}_{\mathrm{ME}}$ is defined as $\boldsymbol{\alpha} = \boldsymbol{\epsilon}\boldsymbol{\alpha}_{\mathrm{ME}}$, where $\boldsymbol{\epsilon}$ is the electric permittivity tensor of the material (Osaretin and Rojas, 2010; Vopson et al., 2017). In experimental settings and under closed circuit boundary condition, polarization is often determined by measuring electric charges. This is due to the reason that when the electric field is zero, electric displacement and electric polarization are equivalent. Similarly, here, we perform a thought experiment and define the effective ME voltage coupling coefficient for HMSE $\alpha_{\mathrm{ME}}^{\mathrm{eff}}$ as

$$\alpha_{\mathrm{ME}}^{\mathrm{eff}} = \frac{\mu_0}{\epsilon^{\mathrm{eff}}}\frac{\partial D_t}{\partial b^{\mathrm{app}}}, \tag{48}$$

where ϵ^{eff} is determined from following equation

$$\frac{H_t + H_b}{\epsilon^{\mathrm{eff}}} = \frac{H_t}{\epsilon_t} + \frac{H_b}{\epsilon_b}. \tag{49}$$

The effective magnetoelectric voltage coefficient of the material can also be written in terms of the output charges $\Delta Q = D_t A$ and the effective capacitance of the material $C^{\mathrm{eff}} = \frac{\epsilon^{\mathrm{eff}} A}{H}$:

$$\alpha_{\mathrm{ME}}^{\mathrm{eff}} = \frac{1}{C^{\mathrm{eff}} H}\frac{\partial(\Delta Q)}{\partial h^e}, \tag{50}$$

where h^e is the external magnetic field ($\mathbf{h}^{\mathrm{e}} = h^e \mathbf{e}_X$), A is the surface area of the electrodes and $H = H_t + H_b$ is the total thickness of the material. Effective voltage coefficient for the hard magnetic soft electret (shown in Fig. 3) is derived by substituting Eq. (42),

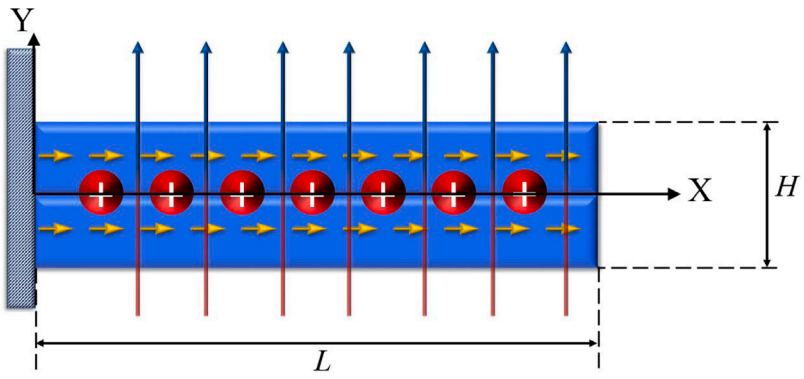

Fig. 4. Schematic of HMSE material that undergoes bending deformation in response to applied magnetic field. The gold arrows show the direction of residual flux density and red circles are electric charges.

(43) and (46) into Eq. (48)

$$\alpha_{\mathrm{ME}}^{\mathrm{eff}} = \frac{1}{\epsilon^{\mathrm{eff}}} \frac{q_0 H_t H_b \epsilon_b \epsilon_t}{(H_t \epsilon_b + H_b \epsilon_t)^2} \times \frac{1}{3} \left(\frac{B_b^r}{G_b} - \frac{B_t^r}{G_t} \right). \tag{51}$$

If the bottom layer does not deform in response to the magnetic field, $\alpha_{\mathrm{ME}}^{\mathrm{eff}}$ can be further simplified as

$$\alpha_{\mathrm{ME}}^{\mathrm{eff}} = -\frac{1}{\epsilon^{\mathrm{eff}}} \frac{q_0 H_t H_b \epsilon_b \epsilon_t}{(H_t \epsilon_b + H_b \epsilon_t)^2} \times \frac{B_t^r}{3G_t}. \tag{52}$$

Several interesting aspects may be noted in Eq. (52). First, the ME voltage coupling coefficient of the HMSE is *independent* of external magnetic field. Therefore, as external field approaches zero, $\alpha_{\mathrm{ME}}^{\mathrm{eff}}$ remains unchanged. This behavior is in contrast with the behavior of ME composites and SMSEs where their ME voltage coupling coefficient vanishes at zero external magnetic field. Also, Eq. (52) shows $\alpha_{\mathrm{ME}}^{\mathrm{eff}} \propto B^r$ for HMSEs while we have shown that for SMSEs $\alpha_{\mathrm{ME}}^{\mathrm{eff}} \propto \mu_0 h^e$. This implies that the voltage coupling coefficient of a HMSE with $B^r \sim 1\mathrm{T}$ under external field $\sim 1\mathrm{mT}$ is three orders of magnitude larger than a SMSE material under same external magnetic field.

4.2. Flexure deformation and magnetoelectricity

Flexure is arguably the most suitable deformation mode for energy harvesting and therefore it is of interest to explore the ME effect under bending. We also remark that the resonance frequency of the bending model is smaller than for tension and compression. Finally, since bending is inherently a non-uniform deformation process, a strong electromechanical coupling can be generated in electret materials (Rahmati et al., 2019) which may then amplify the magnetoelectric response. Pertaining to this, we note that it is not easily possible to create bending deformation with SMSE materials however this is quite simple in the context of hard magnetic soft materials as already demonstrated in past work (Zhao et al., 2019). The flexure problem for HMSE materials is rather difficult to solve analytically however we attempt an approximate solution using Euler–Bernoulli beam theory assumptions (Fig. 4). We will comment on the accuracy of the results in the next section where we will present numerical solutions.

Consider the hard magnetic material shown in Fig. 4. The residual magnetic flux density of the material is uniformly aligned along the axis of the beam $\widetilde{\mathbf{B}}^r = B^r \mathbf{e}_X$. Due to the pattern of residual magnetic dipoles, this particular configuration undergoes bending deformation in response to applied magnetic field across the thickness of the material. We assume the deformation is small ($|\nabla \mathbf{u}| \ll 1$) and the effect of the Maxwell stress is negligible. The applied magnetic flux density is denoted by $\mathbf{b}^{\mathrm{app}} = b^{app} \mathbf{e}_Y$. Using Euler–Bernoulli beam theory, the displacement $\mathbf{u}$ can be expressed as

$$\mathbf{u} = -Y \frac{\partial u_Y}{\partial X} \mathbf{e}_X + u_Y \mathbf{e}_Y. \tag{53}$$

We assume a unit width for the beam and use Euler–Bernoulli theory to express the internal energy of the material as

$$U[u_Y] = \int_0^L \left(\frac{3}{2} GI \left(\frac{\partial^2 u_Y}{\partial X^2} \right)^2 - \frac{H}{\mu_0} \frac{\partial u_Y}{\partial X} b^{app} B^r \right) \mathrm{d}X. \tag{54}$$

The moment of inertia for beam with unit width is $I = \frac{1}{12}H^3$. The equilibrium equations of the beam is derived using standard calculus of variation.

$$\begin{aligned}&\frac{\mathrm{d}U[u_Y+\varepsilon\eta]}{\mathrm{d}\varepsilon}\bigg|_{\varepsilon=0} = \int_0^L \left(3GI\frac{\partial^2 u_Y}{\partial X^2}\frac{\partial^2\eta}{\partial X^2} - \frac{H}{\mu_0}\frac{\partial\eta}{\partial X}b^{app}B^r\right)\mathrm{d}X = \\ &\left(3GI\frac{\partial^2 u_Y}{\partial X^2}\frac{\partial\eta}{\partial X}\right)\Big]_0^L - \left(3GI\frac{\partial^3 u_Y}{\partial X^3}\eta + \frac{H}{\mu_0}b^{app}B^r\eta\right)\Big]_0^L \\ &+ \int_0^L \left[\eta\frac{\partial}{\partial X}\left(3GI\frac{\partial^3 u_Y}{\partial X^3} + \frac{1}{\mu_0}b^{app}B^r\right)\right]\mathrm{d}X = 0.\end{aligned} \tag{55}$$

Thus, the deflection of cantilever beam may be obtained by solving the following system of equations

$$\begin{aligned}&\frac{\partial}{\partial X}\left(3GI\frac{\partial^3 u_Y}{\partial X^3} + \frac{1}{\mu_0}b^{app}B^r\right) = 0,\\ &u_Y(X=0) = \frac{\partial u_Y}{\partial X}\bigg|_{X=0} = \frac{\partial^2 u_Y}{\partial X^2}\bigg|_{X=L} = 0,\\ &\left(3GI\frac{\partial^3 u_Y}{\partial X^3} + \frac{H}{\mu_0}b^{app}B^r\right)\bigg|_{X=L} = 0.\end{aligned} \tag{56}$$

Considering a uniform magnetic field and uniform residual magnetic field, the magnetic field induced deflection of the beam can simply be obtained by solving system of Eqs. (56)

$$\frac{u_Y}{L} = 2(AR)^2\frac{b^{app}B^r}{G\mu_0}\left((\frac{x}{L})^2 - \frac{1}{3}(\frac{x}{L})^3\right), \tag{57}$$

where $AR = L/H$ is the aspect ratio of the material. Thus, the local curvature of the beam $\kappa = \frac{\partial^2 u}{\partial x^2}$ is determined as

$$\frac{\partial^2 u}{\partial x^2} = \frac{b^{app}B^r}{G\mu_0}\frac{4L}{H^2}\left(1 - \frac{x}{L}\right). \tag{58}$$

We cannot use the solution provided in this section to determine output charge of a hard magnetic soft electret under bending deformation because it was a linear decoupled problem. The relation between magnetic field and curvature is illustrated in Eq. (58). To obtain an analytical relation between the output charge and magnetic field, the fully coupled problem has to be solved which is a rather difficult nonlinear problem. However, Rahmati et al. (2019) presented a simple relationship between curvature and output charge for an electret under pure bending. According to their model, the output charge is related to curvature κ through $D^t = \frac{1}{4}q_0 H\kappa$ where q_0 is the surface charge density at the interface of two materials. Therefore, for illustrative purposes, the scale of the output charge for a hard magnetic soft electret with uniform distribution of residual magnetic flux density under bending deformation can be roughly approximated as

$$D^t \propto \frac{b^{app}B^r}{G\mu_0}ARq_0, \tag{59}$$

and, as a result, we have

$$\alpha_{\mathrm{ME}} \propto (AR)\frac{B^r}{G}\frac{q_0}{\epsilon^{\mathrm{eff}}}. \tag{60}$$

Eq. (60) shows that the ME voltage coupling coefficient of the material shown in Fig. 4 linearly depends on the aspect ratio of the material. We may infer the following from this simple approximate result that the ME voltage coupling coefficient of the HMSE under bending deformation is independent of external magnetic field. In addition, by comparing Eqs. (52) and (60) it is seen that the ME voltage coupling of the material is linearly increased by increasing interface charges or by increasing residual magnetic flux density for both bending and tension compression deformation. Also, the relation (60) shows that the ME voltage coupling coefficient of the HMSE under bending deformation linearly depends on the aspect ratio of the material. This is in contrast to the ME voltage coupling coefficient of the HMSE under tension/compression deformations. As the length of the material can be several orders of magnitude larger than the thickness of the material, the ME voltage coupling coefficient of the HMSE under bending deformation can be several orders of magnitude larger than ME voltage coupling coefficient of the HMSE under tension/compression deformation.

4.3. Shape programmable property of HMSEs

Hard magnetic soft elastomers can be quite easily programmed to develop any desirable deformation in response to external magnetic field by designing the residual flux density profile of the material (Gong et al., 2020). As the ME response of the material directly depends on the actuation strain in these materials, the ME response too can be designed by suitably programming the residual flux density. The profile of the residual flux density in these materials depends on the deformation imposed on the material during magnetization step. In this section, we will show that if the material is held in a bent configuration during the magnetization step, the residual magnetic profile of the material will reflect this bent shape. This behavior can be generalized to any desired pattern of deformation. We have chosen flexure deformation mode for illustrative purpose because our theoretical calculations showed that the ME effect mediated with bending deformation can lead to a significantly strong ME effect (Eq. (60)). We calculate the profile for

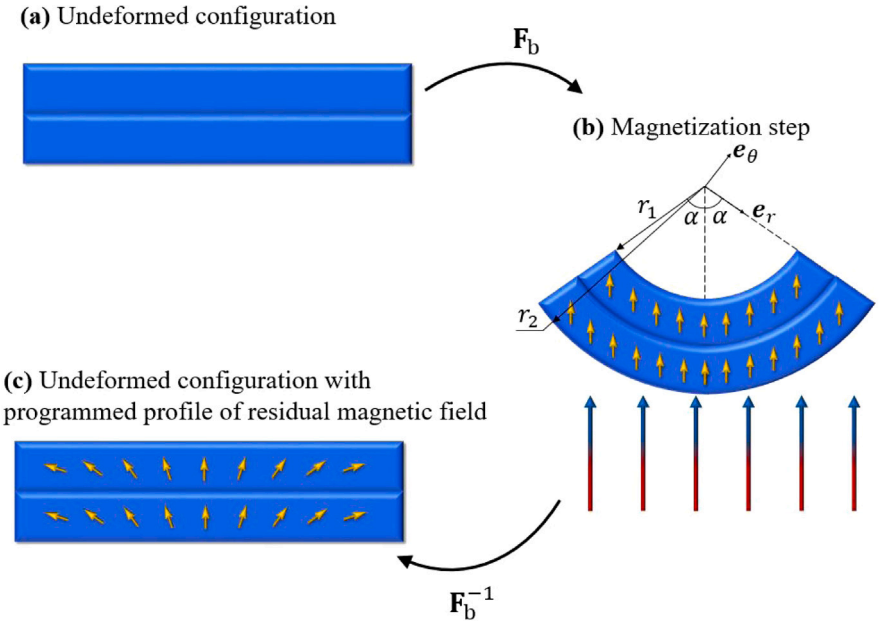

Fig. 5. The steps for creating a programmable hard magnetic soft electret. (a) Initially the average magnetization of the material is zero and magnetic micro-particles are randomly oriented. (b) The desired deformation (which is bending in this case) is induced in material by applying bending moment M and the pre-magnetization magnetic field is applied to the material. The magnetic particles re-align themselves with external field. The gold arrows show the orientation of magnetic particles and arrows with gradient color show the direction of external magnetic field. (c) The imposed deformation and applied magnetic field is removed but the magnetic particles retain their orientation.

residual magnetic flux density of the material in this section and subsequently use a numerical approach (next section) to evaluate the ME response.

Fig. 5 illustrates the three steps for the creation of a PHMSE which bends in response to magnetic field. Initially, the magnetic dipoles of the magnetic micro-particles inside the material are randomly oriented and the residual magnetic flux density of the material is zero(Fig. 5a). In the second step, a pure bending deformation is imposed to the material and a large external magnetic field is imposed on the structure(Fig. 5b). The deformation gradient tensor for this deformation is denoted by $\mathbf{F}_b$. In this step, magnetic dipoles of the micro particles rotate and align themselves with the external field and, as a result, a net magnetic flux density is created inside the material. The re-alignment of the magnetic dipoles of the magnetic micro particles itself does not create any substantive deformation in the material.This re-alignment is due to the rotation and magnetic alignment of the magnetic dipoles and not because of the mechanical rotation of magnetic micro-particles. Due the high coercivity and high residual magnetic flux density of NdFeB micro particles, subsequent to the alignment, the magnetization profile remains stable even after the magnetization magnetic field of step two has been turned off. Thus, in the last step, we remove the magnetic field used to magnetize the material and reverse the deformation. The magnetic micro particles are anchored to the matrix material and they rotate as the material element rotates. Therefore, the reversed deformation developed from step two to step three leads to creation of the residual magnetic flux density profile shown in Fig. 5c.

We denote the magnetic flux density in step three by $\widetilde{\mathbf{B}}^r$. The residual magnetic flux density in the configuration shown in the step two is denoted by $\mathbf{b}^{\text{mag}}$ and is expressed as

$$\mathbf{b}^{\text{mag}} = -B^r\cos(\theta)\mathbf{e}_r + B^r\sin(\theta)\mathbf{e}_\theta \tag{61}$$

The magnetic flux densities $\mathbf{b}^{\text{mag}}$ and $\widetilde{\mathbf{B}}^r$ are related to each other through the third of Eq. (3) $\widetilde{\mathbf{B}}^r = \det(\mathbf{F}_b)\mathbf{F}_b^{-1}\mathbf{b}^{\text{mag}}$. Therefore, we need to determine the deformation $\mathbf{F}_b$ in order to determine the profile for magnetization flux density. The analytical solution for large elastic deformation of material under pure bending was first presented by Rivlin (1949). Motivated by Rivlin's solution, recently we have derived the solution for bending deformation of electret materials (Rahmati et al., 2019). We simply present the final expression for $\mathbf{F}_b$. The reader is referred to Rivlin (1949) and Rahmati et al. (2019) for further details.

The material point in the undeformed configuration (step one and three) are denoted by $\mathbf{X} = X\mathbf{e}_X + Y\mathbf{e}_Y$. The spatial points in step two are denoed by $\mathbf{r} = r\mathbf{e}_r$. For a deformation that is a pure symmetric plane strain bending such that material point each plane originally located in plane with normal $\mathbf{e}_Y$ (resp. $\mathbf{e}_X$) will transfer to a plane with normal $\mathbf{e}_r$ (resp. $\mathbf{e}_\theta$) as a result of this deformation. The desired bending angle α (see Fig. 5b) is achieved by controlling the bending moment applied to the material. Stipulating incompressibility, the deformation gradient $\mathbf{F}_b$ is determined as

$$\mathbf{F}_b = \frac{L}{2\alpha \times r(Y)}\mathbf{e}_r \otimes \mathbf{e}_Y + \frac{2\alpha \times r(Y)}{L}\mathbf{e}_\theta \otimes \mathbf{e}_X, \tag{62}$$

where

$$r(Y)=\sqrt{(r_2^2-r_1^2)\frac{Y}{H}+\frac{r_2^2+r_1^2}{2}},\qquad \theta(X)=\frac{(2Y-L)\alpha}{L}. \tag{63}$$

and r_1 and r_2, respectively, are radii of curved surfaces initially located at $Y=0$ and $Y=H$ (Fig. 5b). For a neo-Hookean constitutive response and traction-free boundary surfaces normal to $\mathbf{e}_r$, r_1 and r_2 may be determined by solving the following nonlinear system of algebraic equation

$$\frac{L}{\alpha}=\frac{r_2^2-r_1^2}{H},\qquad \left(\frac{r_2-r_1}{H}\right)^4=\frac{16\frac{r_2^2}{r_1^2}}{\left(\frac{r_2}{r_1}+1\right)^4}. \tag{64}$$

Finally, the magnetic flux density at each point of PHMSE is determined substituting Eqs. (61) and (62) into third of Eq. (3)

$$\widetilde{\mathbf{B}}^r=\frac{B^r L}{2\alpha r(Y)}\sin\left[\theta(X)\right]\mathbf{e}_X-\frac{2B^r\alpha r(Y)}{L}\cos\left[\theta(X)\right]\mathbf{e}_Y. \tag{65}$$

Clearly, the obtained profile for the residual flux density restores information about the deformed configuration in the magnetization step. We will use this profile in the subsequent section in our numerical simulations. Unless otherwise stated, we set value of $B^r=0.0767\ T$ and use the profile given in Eq. (65) in all simulation results.

5. Numerical results, comparison with experiments and discussion

In this section, we use the formulation presented in Section 3 to simulate the ME behavior of HMSE and PHMSEs using the open source finite element code, FEniCS. In order to check accuracy of our computational model, first we compare our results with the available theoretical, experimental and numerical results. Then, we present solutions for the bending deformation of HMSEs and PHMSEs. Throughout this section, we have assumed that the external magnetic field is constant and the simplified form of the magnetic Maxwell stress (26) has been used. We use the incompressible neo-Hookean constitutive law given in the Eq. (39) and plane strain conditions. Unless otherwise stated, Young's elastic modulus of the material is set to 55 KPa, the magnitude of the residual flux density is $B^r=0.0767$, the electric permittivity of the material is equal to $\epsilon=5.0676\epsilon_0$ and the interface charge density is $q_0=0.0488\ \text{mC/m}^2$. Also, the length and the thickness of the sample, respectively, are set to be $L=22$ mm, $H=1.85$ mm. These numerical values are consistent with the material fabricated and examined by the Qian Deng Research Group.

5.1. The bending deformation of hard magnetic soft elastomer without electrets

As the first step of our analysis, we simulate the material shown in the Fig. 4 without considering effects of external charges ($\widetilde{\rho}_e=0$). The residual flux density is uniformly aligned with the axis direction of the material and an external magnetic field is applied across the thickness of the material. This problem has been solved by Zhao et al. (2019) both numerically (using an ABAQUS UMAT) and experimentally. Fig. 6 shows that there is an excellent agreement between our finite element results and the experimental and simulation results given by Zhao et al. (2019). Fig. 6(a) compared the deformed configuration from our simulation with the experimental observations for two materials with two different aspect ratios under the same magnetic field. Also, Fig. 6(b) shows that the deflection versus dimensionless magnetic field for materials with different aspect ratios and we see excellent agreement with Zhao et al. (2019).

5.2. Magnetoelectric energy harvesting using parallel plate capacitor made of hard magnetic soft elastomer

In the next step, we illustrate the ability of electric energy harvesting by applying an external magnetic field to a parallel plate capacitor made of hard magnetic soft elastomer and compare the numerical results with analytical results. Consider the material shown in Fig. 7(a) where residual magnetic field is aligned parallel with the thickness direction of the material. A voltage difference V has been applied across the thickness of the material. Once a magnetic field is applied to the material along the thickness direction and in the opposite direction with respect to residual field, the material tends to compress. This compression increases the electric field inside the material and enables material to do work on the boundary electric device. This work can be determined as

$$W=-\int_{\Gamma_D}\left[\xi_b\left(\widetilde{\mathbf{D}}-\widetilde{\mathbf{D}}^i\right)\cdot\mathbf{N}\right], \tag{66}$$

where $\widetilde{\mathbf{D}}^i=\lim_{\mathbf{B}^{app}\to\mathbf{0}}\widetilde{\mathbf{D}}$. The value of W can be determined analytically. The procedure for analytical solution is very similar to what was mentioned in Section 4.1. The only difference is that, here, we enforce a plane strain condition to be consistent with numerical calculations. Under plane strain condition, equilibrium equation is written as

$$(\lambda^4-1)-\lambda^3\frac{\widetilde{\mathbf{B}}^r\cdot\mathbf{b}^{app}}{G\mu_0}+\frac{\epsilon}{G}\left(\frac{V}{H}\right)^2=0, \tag{67}$$

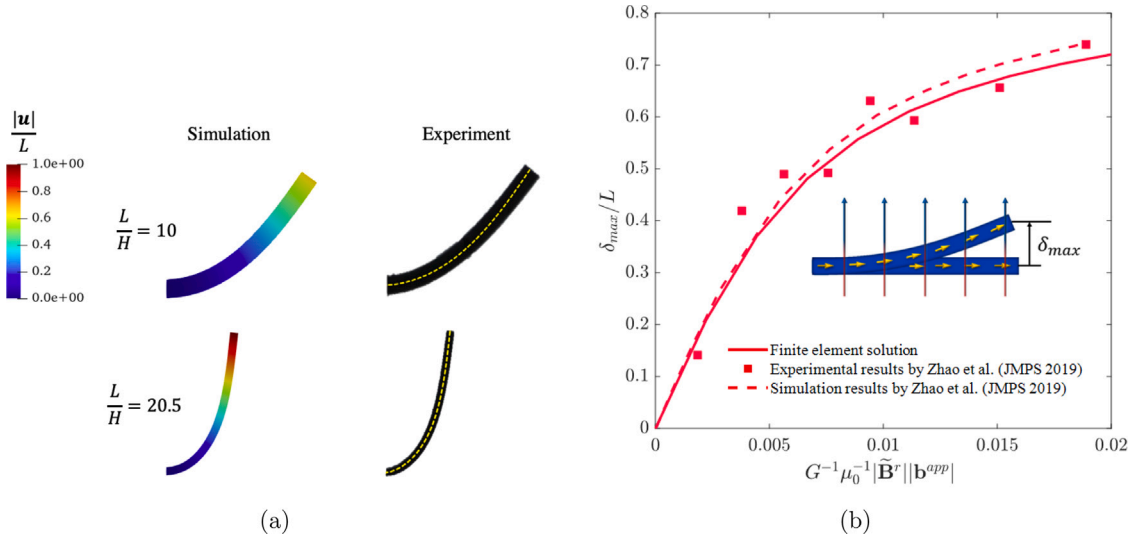

Fig. 6. Comparison of the current numerical solution with experimental and simulation results given by Zhao et al. (2019). (a)The deformed configuration observed in the simulation versus the experiment for $\frac{|\mathbf{b}^r||\mathbf{b}^{app}|}{G\mu_0} = 0.0094$ and $AR = \frac{L}{H} = 10$. Color contours show the magnitude of dimensionless displacement. (b) Comparison of simulation and experimental results for vertical displacement of the tip of the beam under different external magnetic fields.

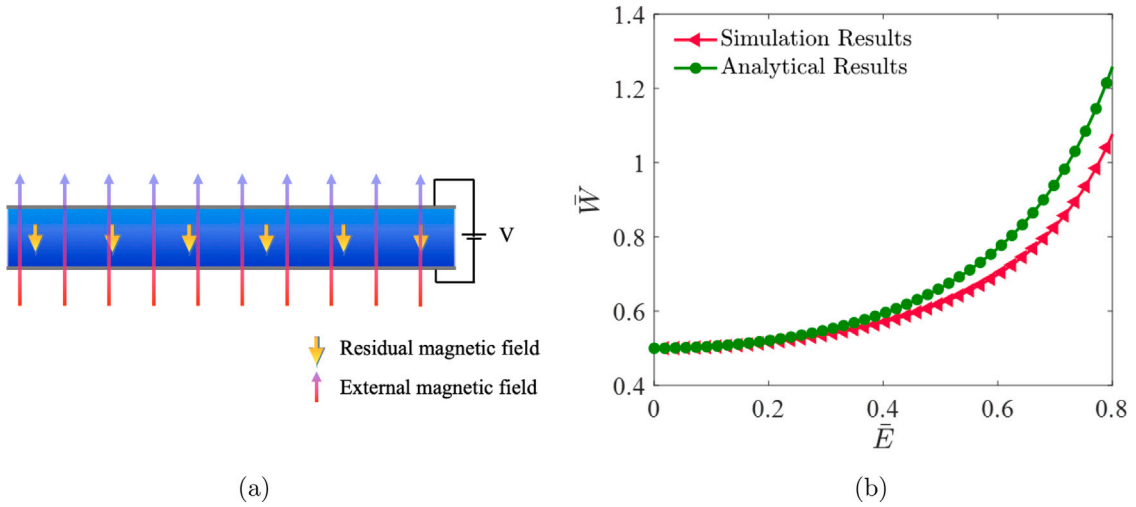

Fig. 7. The electric energy harvesting by applying magnetic field to a parallel plate capacitor made of hard magnetic soft elastomer. (a) Schematics of a material under electric voltage difference V. (b) Comparison of theoretical results and simulation results for the electric energy harvested by applying a magnetic field to a parallel plate capacitor made of hard magnetic soft elastomer.

where λ is the stretch along the thickness direction. Assuming $|\lambda - 1| \ll 1$, above equation can be linearized and solved for λ. The calculated value of the stretch can be substituted in Eq. (66) to determine energy harvested at the boundary. Therefore, the electric work done on the boundary electric device for $G^{-1}\mu_0^{-1}|\mathbf{b}^r||\mathbf{b}^{app}| \ll 1$ is determined as

$$\bar{W} = \frac{W}{A} \times \left(\epsilon \frac{V}{H} \times \frac{|\mathbf{b}^r||\mathbf{b}^{app}|}{G^{-1}\mu_0^{-1}} \right)^{-1} \approx \frac{8 - 4\bar{E}^2}{\left(4 - 3\bar{E}^2\right)^2}, \tag{68}$$

where A is the top surface area of the material. Also, dimensionless electric energy $\bar{E}$ is defined as

$$\bar{E} = \frac{V}{H}\sqrt{\frac{\epsilon}{G}} \tag{69}$$

The relation (68) has been used to generate Fig. 7(b). Good agreement is seen between our analytical results and simulations. Also, it is clear in the relation (68) that $\bar{W}$ is independent of the magnetic field and only depends on dimensionless electric field. Our numerical solution for compression problem also shows that $\bar{W}$ is independent of magnetic field. Therefore, we can conclude

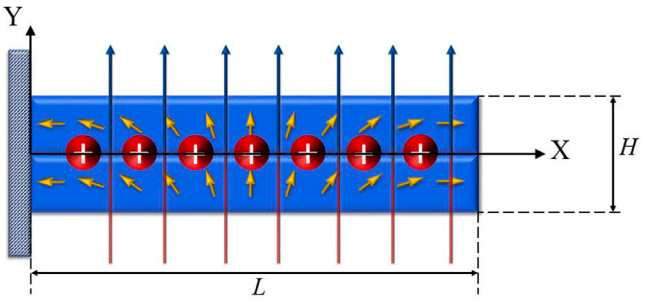

Fig. 8. Schematic of the PHMSE. The gold arrows show the direction of residual magnetic field.

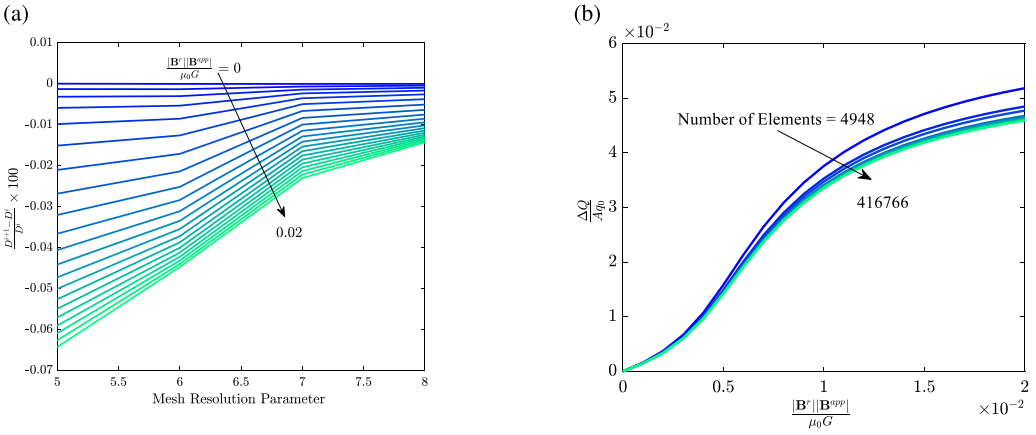

Fig. 9. Mesh convergence study.

that magnetic field will not change $\bar{W}$ in the compression problem under small strain assumption. In the other words, according to Eq. (68), the amount of electric energy can be harvested at the boundary W *linearly* increases as dimensionless magnetic field $G^{-1}\mu_0^{-1}|\mathbf{b}^r||\mathbf{b}^{app}|$ increases.

5.3. The magnetoelectric effect in PHMSEs

In the next step, we simulate the behavior of the PHMSE shown in Fig. 8. The profile of the residual magnetic flux density is given in the Eq. (65). We assume the material is cantilevered from the left end and a magnetic field across its thickness is applied ($\mathbf{h}^e = h^e\mathbf{e}_Y$). The short circuit electrical boundary condition $\xi = 0$ has been applied to surfaces $Y = \pm H/2$. The deformation is fully constrained on the cantilever side of the beam ($X = 0$). Unless otherwise stated, a layer of external charges with the surface charge density $q_0 = -0.048$ mC/m^2 has been inserted to the material at $Y = 0$. Due to existence of interface charges, the electric potential inside the material is not zero even in absence of the external loading. Therefore, we have to compare the solution in two states, in presence and absence of the externally applied magnetic field, in order to determine generated voltage inside the material. We identify the generated electric potential $\xi - \xi^0$, where ξ^0 is the electric potential of the system determined at $\mathbf{h}^e = \mathbf{0}$. Similarly, the output charge ΔQ over surface area of the electrode A can be determined as

$$\frac{\Delta Q}{A} = \frac{1}{L}\int_0^L \left(D^f(X) - D^i(X)\right) \mathrm{d}X, \tag{70}$$

where D^f is defined as $D^f = (\widetilde{\mathbf{D}} \cdot \mathbf{e}_Y)|_{Y=H}$ determined at $\mathbf{h}^e = h^e\mathbf{e}_Y$. Also, D^t is defined as $D^t = (\widetilde{\mathbf{D}} \cdot \mathbf{e}_Y)|_{Y=H}$ determined at $\mathbf{h}^e = \mathbf{0}$. The ME voltage coupling coefficient is calculated substituting Eq. (70) into Eq. (50)

$$\alpha_{\mathrm{ME}}^{\mathrm{eff}} = \frac{1}{\epsilon^{eff}}\frac{\partial}{\partial h^e}\left(\frac{1}{L}\int_0^L D^f(X)\mathrm{d}X\right). \tag{71}$$

We have ensured mesh convergence for our FENICS calculations (see Fig. 9). Fig. 10 compares our simulation results with experimental observations for this problem and good agreement is found. The material has the dimensions of $35 \times 12 \times 0.8$ mm, Young's elastic modulus of 59.4 KPa and density of 1980 Kg/m^3. As Figs. 10a and 10b show, in this experiment, the material is hanging from a top surface where displacement was fully constrained. We have included effect of gravity in our simulations. The shape programmable ability of the PHMSE is illustrated in this figure where a uniform magnetic field leads to a non-uniform

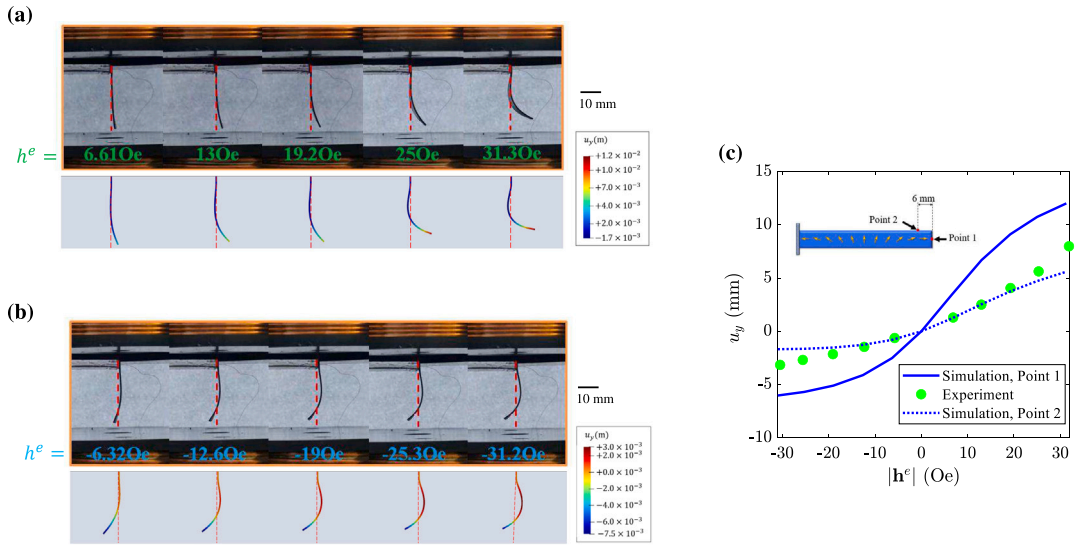

Fig. 10. The deformed configuration observed in the experiment versus the deformed configuration obtained using FE model for the PHMSE under different (a) positive and (b) negative magnetic fields. (c) Comparison of experimental and numerical results for deflection of the material under different values of the magnetic field.

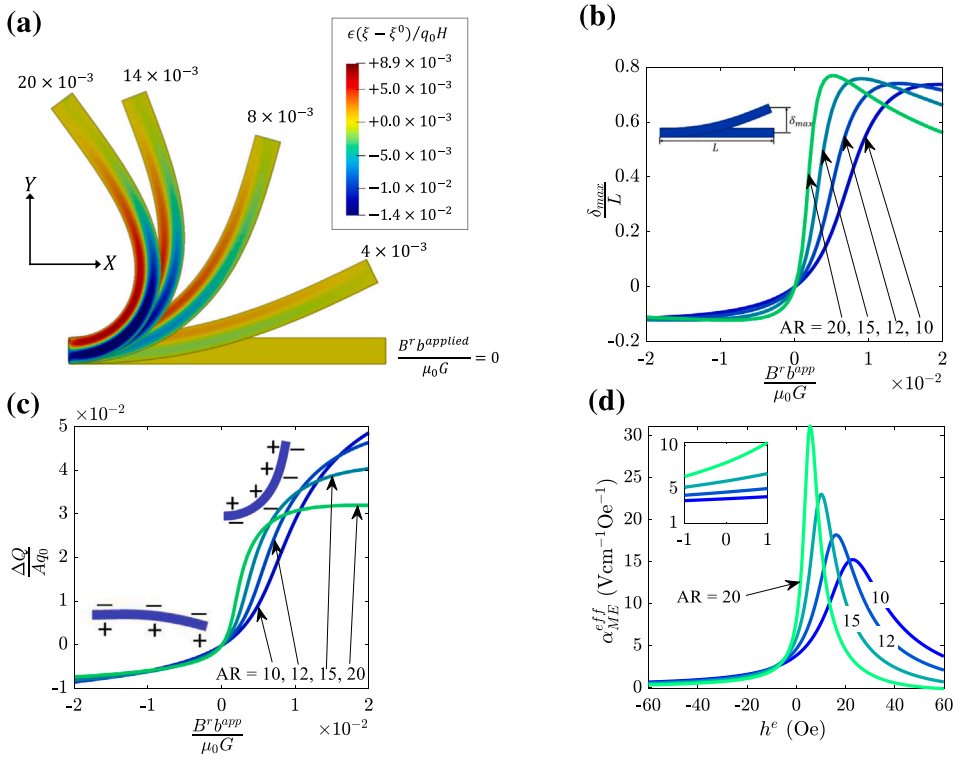

Fig. 11. The numerical results showing ME effect in PHMSE. (a) Contour plots showing changes observed in the distribution of electric potential in response to the applied magnetic field. (b) Dimensionless deflection of the tip point for beams with different aspect ratios. (c) Dimensionless output charges harvested at two electrodes attached to the surface of material in response to applied magnetic field. (d) The ME voltage coupling coefficient versus applied external magnetic field.

deformation. Also, it is clear that the deformation is not symmetric with respect to the magnetic field. This is because the direction of residual magnetic field is not symmetric. Therefore, as the direction of the applied magnetic field is reversed, the direction of the deformation does not reverse completely.

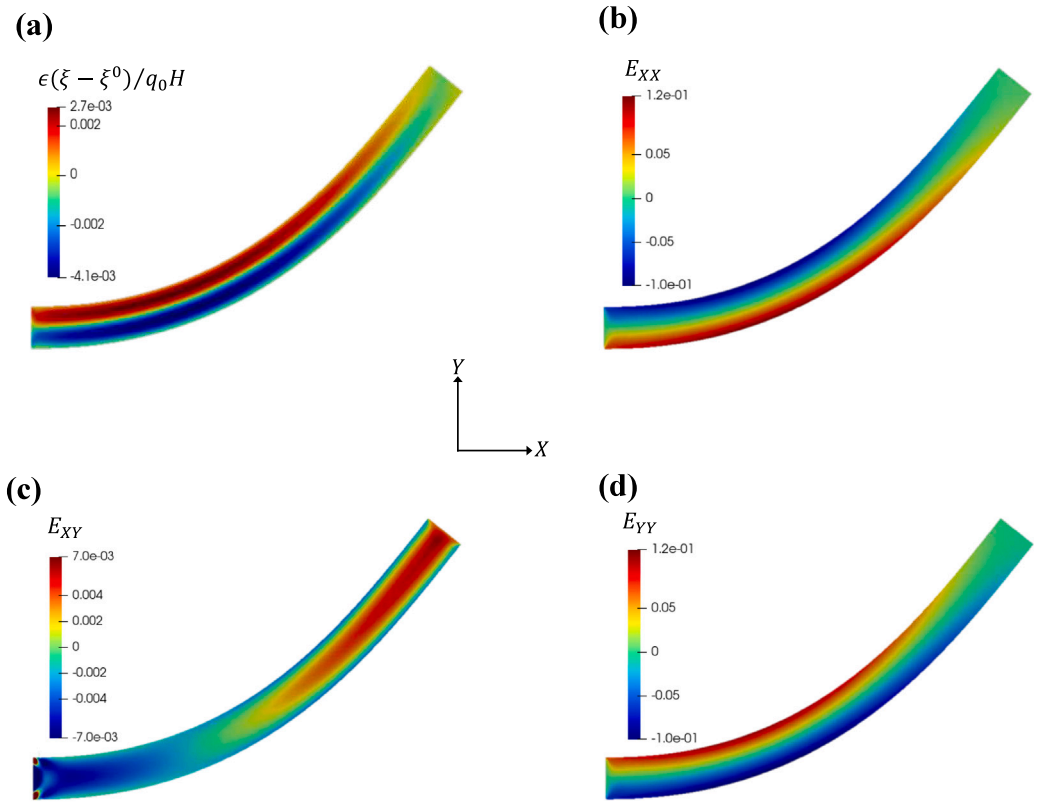

Fig. 12. The contours of (a) dimensionless generated electric potential (b-d) and strain components for PHMSE where $\mathbf{E} = \mathbf{F}^T\mathbf{F} - \mathbf{I}$.

Fig. 11a shows the deformed configuration and contours of generated dimensionless electric potential for different values of magnetic fields. The dimensionless electric potential is defined as $\epsilon(\xi - \xi^0)/(q_0 H)$, where ξ, ϵ, q_0 and H, respectively, are electric potential, electric permittivity, surface charge density at the interface and the thickness of the material. The potential ξ^0 is the electric potential at each point in absence of external magnetic field. This figure shows that the applied magnetic field changes the distribution of electric potential and the electric field is generated within the material in response to applied magnetic. The generated electric field increases as external magnetic field increases. The contours of generated electric potential are compared with strain components in Fig. 12. Evidently, inhomogeneous strain leads to the presence of electric potential difference and this implies that emergence of electric potential difference and ME effect is mediated by strain gradients. It is convenient to achieve magnetoelectric coupling through bending deformation since bending is one of the simplest way to induce strain gradient in the material without using a composite structure (last section).

The dimensionless vertical displacement of the tip point of the beam is shown in Fig. 11b for beams with different aspect ratios (AR = L/H). Also, the dimensionless output charges $\frac{\Delta Q}{A q_0}$ (calculated using (70)) versus applied dimensionless magnetic field $\frac{B^r b^{app}}{\mu_0 G}$ is plotted in Fig. 11c. A larger deflection and output charge is observed for the materials with larger aspect ratios under small magnetic fields. However, as the magnetic field increases, the deflection and output charges increase until they reach a plateau where maximum deflection and output charges have been reached. For beams with greater ARs, the maximum deflection is reached at smaller magnetic fields. In addition, we observe that the deformation (and consequently output charges) is not symmetric with respect to the applied magnetic field. This is because the residual field is not symmetric. Fig. 13 shows a symmetric behavior in HMSEs with residual field uniformly aligned along the axis of the beam ($\widetilde{\mathbf{B}}^r = B^r \mathbf{e}_X$). Fig. 13 shows that for the material with a symmetric alignment of the residual field, imposing external magnetic fields with opposite signs will lead to deflections (Fig. 13b), output charges (Fig. 13b) and magnetoelectric voltage coupling coefficients (Fig. 13c) with the opposite sign.

We show, using Fig. 11, that external magnetic field induces bending and electric charges can be harvested at the electrodes attached to the surface of material in response to the bending. This resulting magnetoelectric effect can be quantified using the magnetoelectric voltage coupling coefficient. The ME voltage coupling coefficient of the PHMSE is numerically calculated using relation (71). The voltage coupling coefficients versus magnetic field for PHMSEs with different aspect ratios are plotted in Fig. 11d. A giant value (greater than 1 $\text{Vcm}^{-1}\text{Oe}^{-1}$) for voltage coupling coefficient of the material is reported at zero external magnetic field. The ME voltage coupling at zero magnetic field increases as the aspect ratio increases. This shows that PHMSEs not only enable substantially large ME coupling but they make it unnecessary to have a bias magnetic field. Thus hard magnetic soft electret form a unique class of materials which provide soft and biocompatible magnetoelectric property which is significantly sensitive to

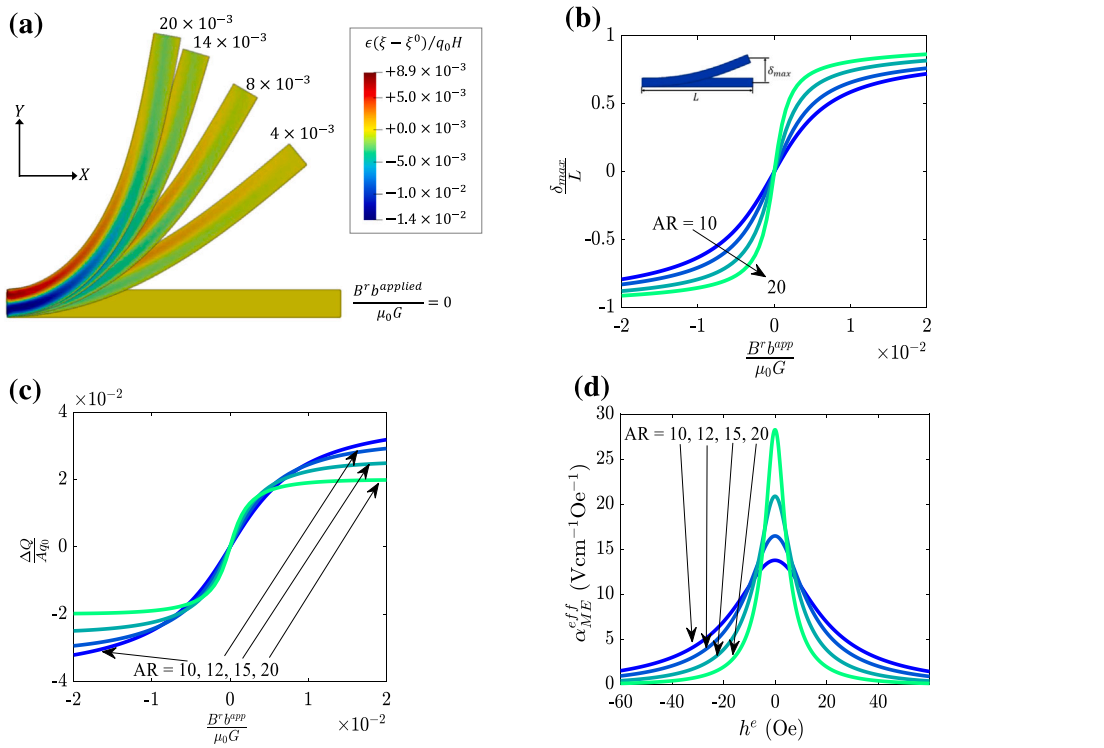

Fig. 13. The numerical results showing ME effect in hard magnetic soft electrets with uniform residual magnetic field. (a) Contour plots showing changes observed in the distribution of electric potential in response to the applied magnetic field for a beam with aspect ratio of AR = 15. (b) Dimensionless deflection of the beam. (c) Dimensionless charges harvested at two electrodes attached to the surface of material in response to applied magnetic field. (d) The magnetoelectric voltage coupling coefficient versus applied external magnetic field.

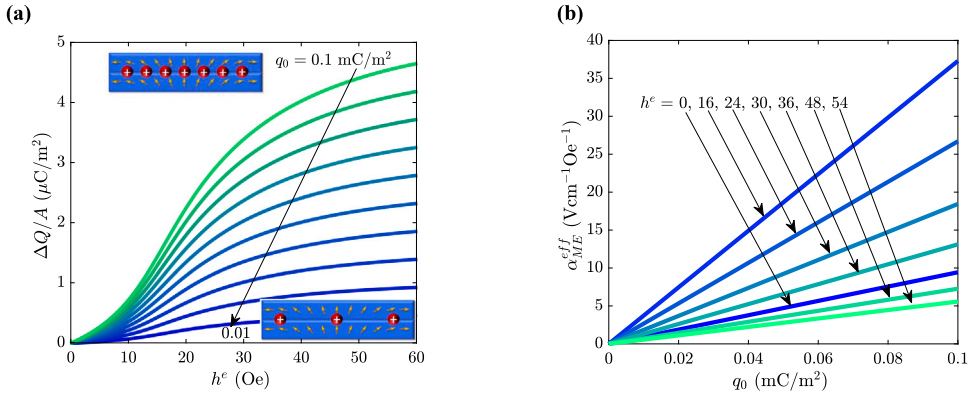

Fig. 14. The effect of surface charge density in ME effect in PHMSEs under bending deformation. (a) FE results for electric charge harvested versus external magnetic field for different values of interface charge density. (b) FE results for the ME voltage coupling coefficient versus surface charge density of the interface.

weak magnetic fields. This value is even comparable with highest values of the ME voltage coupling coefficients of polymer based magnetoelectric composites.

Effect of interfacial charge density. There is a direct relationship between interface charge density and the amount of charge that can be harvested from the PHMSEs under magnetic field induced bending deformation. Results obtained from our finite element model shows that the larger the interface surface charge density is, more electrical energy can be harvested (14a). The voltage coupling coefficient versus interface surface charge density for PHMSEs under different external magnetic field is plotted in Fig. 14b. A linear relation between ME voltage coupling coefficient of the material and interface charge density is observed.

Effect of deformation resulting from the magnetization step. The magnetoelectric effect in PHMSEs may be impacted by the initial curvature induced in the material in the magnetization stage. The initial curvature is controlled by bending angle α (see

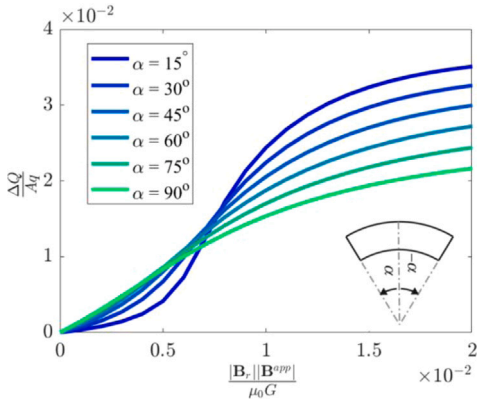

Fig. 15. The effect of bending angle in the pre-magnetization stage on the harvested electric charges of PHMSE. The length of the beam is 35 mm and its thickness is 0.8 mm. Also, $q_0 = 0.1$ mC/m^2.

the inset of Fig. 15) which has a direct impact on the profile of residual magnetic flux density given in Eq. (65). The effect of bending angle in magnetization stage on the ME effect of the PHMSE is studied in the Fig. 15. Evidently, the output charge can be modified by changing the bending angle in the pre-magnetization stage. This is a proof of concept that shows PHMSE materials can be customized to show desired actuation and magnetoelectric effect that may be tailored for a particular application. We remark that past work has shown that hard magnetic soft materials can be easily programmed to actuate into very complex configurations in response to uniform external magnetic field. Thus, very complex electric signals can be produced in response to applied magnetic field (Gong et al., 2020) paving the way for remote transfer of information.

6. Concluding remarks

In summary, we have introduced hard magnetic soft electret materials as a new class of materials which enable large deformation and a strong magnetoelectric coupling in one single material. In sharp contrast to magnetoelectric composite materials and recently developed soft magnetic electret materials, we show that the magnetoelectric effect in hard magnetic electrets is independent of the externally applied magnetic field. Indeed, hard magnetic soft electrets show a significant magnetoelectric coupling at infinitesimal magnetic fields without the need for any bias magnetic field. Our investigation indicates that the room-temperature magnetoelectric voltage coefficient in a simple bi-layer hard magnetic soft electret is as high as 332.7 mVcm^{-1} Oe^{-1} and furthermore can be easily programmed to exhibit a ME effect mediated by desired deformation. A "giant" voltage coupling coefficient of greater than 15.36 Vcm^{-1} Oe^{-1} is possible in elastically homogeneous programmable hard magnetic soft electrets at resonance frequency of 6 Hz when the magnetoelectric effect is mediated by bending deformation. Several avenues for future work are possible: biology c.f. Torbati et al. (2022), topology optimization (Zhao and Zhang, 2022), multiscale computational modeling in analogy with developments in electrostatics (Marshall and Dayal, 2014), temperature sensitive design as done in the context of ferroelectrics (Mbarki et al., 2014), templated structures c.f. Alizadeh et al. (2004), design of soft magnetic material at the chain level using statistical mechanics as done recently in the context of electrostatics (Cohen et al., 2016; Grasinger and Dayal, 2020; Grasinger et al., 2021), exploration of instability mechanisms c.f. Yang et al. (2017), among others.

Declaration of competing interest

The authors declare that they have no known competing financial interests or personal relationships that could have appeared to influence the work reported in this paper.

Data availability

Data will be made available on request.

References

Alameh, Z., Deng, Q., Liu, L., Sharma, P., 2014. Using electrets to design concurrent magnetoelectricity and piezoelectricity in soft materials. J. Mater. Res. 30, 93–100.

Alizadeh, A., Sharma, P., Ganti, S., LeBoeuf, S., Tsakalakos, L., 2004. Templated wide band-gap nanostructures. J. Appl. Phys. 95 (12), 8199–8206.

Annapureddy, V., Palneedi, H., Hwang, G.-T., Peddigari, M., Jeong, D.-Y., Yoon, W.-H., Kim, K.-H., Ryu, J., 2017. Magnetic energy harvesting with magnetoelectrics: an emerging technology for self-powered autonomous systems. Sustain. Energy Fuels 1 (10), 2039–2052.

Apte, A., Mozaffari, K., Samghabadi, F.S., Hachtel, J.A., Chang, L., Susarla, S., Idrobo, J.C., Moore, D.C., Glavin, N.R., Litvinov, D., et al., 2020. 2D electrets of ultrathin moO2 with apparent piezoelectricity. Adv. Mater. 32 (24), 2000006.

Babuška, I., 1971. Error-bounds for finite element method. Numer. Math. 16 (4), 322–333.
Bauer, S., Gerhard, R., Sessler, G.M., 2004. Ferroelectrets: Soft electroactive foams for transducers.
Bhavanasi, V., Kumar, V., Parida, K., Wang, J., Lee, P.S., 2016. Enhanced piezoelectric energy harvesting performance of flexible PVDF-TrFE bilayer films with graphene oxide. ACS Appl. Mater. Interfaces 8 (1), 521–529.
Bhoi, K., Mohanty, H., Abdullah, M.F., Pradhan, D.K., Babu, S.N., Singh, A., Vishwakarma, P., Kumar, A., Thomas, R., Pradhan, D.K., et al., 2021. Unravelling the nature of magneto-electric coupling in room temperature multiferroic particulate (PbFe 0.5 Nb 0.5 O 3)–(Co 0.6 Zn 0.4 Fe 1.7 Mn 0.3 O 4) composites. Sci. Rep. 11 (1), 1–17.
Bibes, M., Barthélémy, A., 2008. Towards a magnetoelectric memory. Nature Mater. 7 (6), 425–426.
Bitla, Y., Chu, Y.-H., 2018. Development of magnetoelectric nanocomposite for soft technology. J. Phys. D: Appl. Phys. 51 (23), 234006.
Bouklas, N., Landis, C.M., Huang, R., 2015. A nonlinear, transient finite element method for coupled solvent diffusion and large deformation of hydrogels. J. Mech. Phys. Solids 79, 21–43.
Brezzi, F., 1974. On the existence, uniqueness and approximation of saddle-point problems arising from Lagrangian multipliers. Publications Mathématiques et Informatique de Rennes (S4), 1–26.
Catalan, G., Scott, J.F., 2009. Physics and applications of bismuth ferrite. Adv. Mater. 21 (24), 2463–2485.
Chang, C., Tran, V.H., Wang, J., Fuh, Y.-K., Lin, L., 2010. Direct-write piezoelectric polymeric nanogenerator with high energy conversion efficiency. Nano Lett. 10 (2), 726–731.
Chen, S., Huang, R., Ravi-Chandar, K., 2020. Linear and nonlinear poroelastic analysis of swelling and drying behavior of gelatin-based hydrogels. Int. J. Solids Struct..
Chu, Z., PourhosseiniAsl, M., Dong, S., 2018. Review of multi-layered magnetoelectric composite materials and devices applications. J. Phys. D: Appl. Phys. 51 (24), 243001.
Cianchetti, M., Laschi, C., Menciassi, A., Dario, P., 2018. Biomedical applications of soft robotics. Nat. Rev. Mater. 3 (6), 143–153.
Cohen, N., Dayal, K., DeBotton, G., 2016. Electroelasticity of polymer networks. J. Mech. Phys. Solids 92, 105–126.
Dagdeviren, C., Yang, B.D., Su, Y., Tran, P.L., Joe, P., Anderson, E., Xia, J., Doraiswamy, V., Dehdashti, B., Feng, X., et al., 2014. Conformal piezoelectric energy harvesting and storage from motions of the heart, lung, and diaphragm. Proc. Natl. Acad. Sci. 111 (5), 1927–1932.
Danas, K., Kankanala, S., Triantafyllidis, N., 2012. Experiments and modeling of iron-particle-filled magnetorheological elastomers. J. Mech. Phys. Solids 60 (1), 120–138.
Danas, K., Triantafyllidis, N., 2014. Instability of a magnetoelastic layer resting on a non-magnetic substrate. J. Mech. Phys. Solids 69, 67–83.
de Cea, M., Atabaki, A., Ram, R., 2021. Energy harvesting optical modulators with sub-attojoule per bit electrical energy consumption. Nature Commun. 12 (1), 1–9.
Deng, Q., Liu, L., Sharma, P., 2014a. Electrets in soft materials: Nonlinearity, size effects, and giant electromechanical coupling. Phys. Rev. E 90 (1), 012603.
Deng, Q., Liu, L., Sharma, P., 2014b. Flexoelectricity in soft materials and biological membranes. J. Mech. Phys. Solids 62, 209–227.
Dong, S., Li, J.-F., Viehland, D., 2003. Ultrahigh magnetic field sensitivity in laminates of TERFENOL-D and Pb (Mg1/3 Nb2/3) O3–PbTiO3 crystals. Appl. Phys. Lett. 83 (11), 2265–2267.
Dong, S., Liu, J.-M., Cheong, S.-W., Ren, Z., 2015. Multiferroic materials and magnetoelectric physics: symmetry, entanglement, excitation, and topology. Adv. Phys. 64 (5–6), 519–626.
Dong, M., Wang, X., Chen, X.-Z., Mushtaq, F., Deng, S., Zhu, C., Torlakcik, H., Terzopoulou, A., Qin, X.-H., Xiao, X., et al., 2020. 3D-printed soft magnetoelectric microswimmers for delivery and differentiation of neuron-like cells. Adv. Funct. Mater. 30 (17), 1910323.
Dong, S., Zhai, J., Wang, N., Bai, F., Li, J., Viehland, D., Lograsso, T.A., 2005. Fe–Ga/Pb (Mg 1/3 Nb 2/3) O3–PbTiO3 magnetoelectric laminate composites. Appl. Phys. Lett. 87 (22), 222504.
Eerenstein, W., Mathur, N., Scott, J.F., 2006. Multiferroic and magnetoelectric materials. Nature 442 (7104), 759–765.
Fiebig, M., 2005. Revival of the magnetoelectric effect. J. Phys. D: Appl. Phys. 38 (8), R123.
Fiebig, M., Lottermoser, T., Meier, D., Trassin, M., 2016. The evolution of multiferroics. Nat. Rev. Mater. 1 (8), 1–14.
Fortin, M., Brezzi, F., 1991. Mixed and Hybrid Finite Element Methods. Springer-Verlag, New York.
Garcia-Gonzalez, D., Landis, C.M., 2020. Magneto-diffusion-viscohyperelasticity for magneto-active hydrogels: rate dependences across time scales. J. Mech. Phys. Solids 103934.
Gong, X., Tan, K., Deng, Q., Shen, S., 2020. Athermal shape memory effect in magnetoactive elastomers. ACS Appl. Mater. Interfaces 12 (14), 16930–16936.
Gong, S., Zhang, J., Wang, C., Ren, K., Wang, Z., 2019. A monocharged electret nanogenerator-based self-powered device for pressure and tactile sensor applications. Adv. Funct. Mater. 1807618.
Grasinger, M., Dayal, K., 2020. Statistical mechanical analysis of the electromechanical coupling in an electrically-responsive polymer chain. Soft Matter 16 (27), 6265–6284.
Grasinger, M., Mozaffari, K., Sharma, P., 2021. Flexoelectricity in soft elastomers and the molecular mechanisms underpinning the design and emergence of giant flexoelectricity. Proc. Natl. Acad. Sci. 118 (21), e2102477118.
Guduru, R., Liang, P., Runowicz, C., Nair, M., Atluri, V., Khizroev, S., 2013. Magneto-electric nanoparticles to enable field-controlled high-specificity drug delivery to eradicate ovarian cancer cells. Sci. Rep. 3 (1), 1–8.
Henann, D.L., Chester, S.A., Bertoldi, K., 2013. Modeling of dielectric elastomers: Design of actuators and energy harvesting devices. J. Mech. Phys. Solids 61 (10), 2047–2066.
Hill, N.A., 2000. Why are there so few magnetic ferroelectrics? J. Phys. Chem. B 104 (29), 6694–6709.
Hu, J.-M., Duan, C.-G., Nan, C.-W., Chen, L.-Q., 2017. Understanding and designing magnetoelectric heterostructures guided by computation: progresses, remaining questions, and perspectives. NPJ Comput. Mater. 3 (1), 1–21.
Jackson, J.D., 1999. Classical Electrodynamics. American Association of Physics Teachers.
Kim, Y., Yuk, H., Zhao, R., Chester, S.A., Zhao, X., 2018. Printing ferromagnetic domains for untethered fast-transforming soft materials. Nature 558 (7709), 274–279.
Kopyl, S., Surmenev, R., Surmeneva, M., Fetisov, Y., Kholkin, A., 2021. Magnetoelectric effect: principles and applications in biology and medicine–a review. Mater. Today Bio 100149.
Kuang, X., Wu, S., Ze, Q., Yue, L., Jin, Y., Montgomery, S.M., Yang, F., Qi, H.J., Zhao, R., 2021. Magnetic dynamic polymers for modular assembling and reconfigurable morphing architectures. Adv. Mater. 33 (30), 2102113.
Lage, E., Kirchhof, C., Hrkac, V., Kienle, L., Meyners, D., 2012. Exchange biasing of magnetoelectric composites. Nature Mater. 11 (6), 523–529.
Lefèvre, V., Danas, K., Lopez-Pamies, O., 2017. A general result for the magnetoelastic response of isotropic suspensions of iron and ferrofluid particles in rubber, with applications to spherical and cylindrical specimens. J. Mech. Phys. Solids 107, 343–364.
Lefèvre, V., Danas, K., Lopez-Pamies, O., 2020. Two families of explicit models constructed from a homogenization solution for the magnetoelastic response of MREs containing iron and ferrofluid particles. Int. J. Non-Linear Mech. 119, 103362.
Liang, X., Chen, H., Sun, N.X., 2021. Magnetoelectric materials and devices. APL Mater. 9 (4), 041114.
Liu, L., 2014. An energy formulation of continuum magneto-electro-elasticity with applications. J. Mech. Phys. Solids 63, 451–480.
Liu, L., Sharma, P., 2018. Emergent electromechanical coupling of electrets and some exact relations—The effective properties of soft materials with embedded external charges and dipoles. J. Mech. Phys. Solids 112, 1–24.

Liu, H., Zhong, J., Lee, C., Lee, S.-W., Lin, L., 2018. A comprehensive review on piezoelectric energy harvesting technology: Materials, mechanisms, and applications. Appl. Phys. Rev. 5 (4), 041306.
Logg, A., Mardal, K.-A., Wells, G., 2012. Automated Solution of Differential Equations By the Finite Element Method: The FEniCS Book. Vol. 84, Springer Science & Business Media.
Lottermoser, T., Lonkai, T., Amann, U., Hohlwein, D., Ihringer, J., Fiebig, M., 2004. Magnetic phase control by an electric field. Nature 430 (6999), 541–544.
Lu, L., Ding, W., Liu, J., Yang, B., 2020. Flexible PVDF based piezoelectric nanogenerators. Nano Energy 105251.
Ma, J., Hu, J., Li, Z., Nan, C.-W., 2011. Recent progress in multiferroic magnetoelectric composites: from bulk to thin films. Adv. Mater. 23 (9), 1062–1087.
Malley, S., Newacheck, S., Youssef, G., 2021. Additively manufactured multifunctional materials with magnetoelectric properties. Addit. Manuf. 102239.
Mandal, S., Gollapudi, S., Petrov, V., Srinivasan, G., 2011. Magnetization-graded multiferroic composite and magnetoelectric effects at zero bias. Phys. Rev. B 84.
Mandal, S., Sreenivasulu, G., Petrov, V., Srinivasan, G., 2010. Flexural deformation in a compositionally stepped ferrite and magnetoelectric effects in a composite with piezoelectrics. Appl. Phys. Lett. 96 (19), 192502.
Marshall, J., Dayal, K., 2014. Atomistic-to-continuum multiscale modeling with long-range electrostatic interactions in ionic solids. J. Mech. Phys. Solids 62, 137–162.
Martins, P., Lanceros-MenNdez, S., 2013. Polymer-based magnetoelectric materials. Adv. Funct. Mater. 23 (27), 3371–3385.
Mbarki, R., Baccam, N., Dayal, K., Sharma, P., 2014. Piezoelectricity above the curie temperature? Combining flexoelectricity and functional grading to enable high-temperature electromechanical coupling. Appl. Phys. Lett. 104 (12), 122904.
Mukherjee, D., Bodelot, L., Danas, K., 2020. Microstructurally-guided explicit continuum models for isotropic magnetorheological elastomers with iron particles. Int. J. Non-Linear Mech. 120, 103380.
Mukherjee, D., Rambausek, M., Danas, K., 2021. An explicit dissipative model for isotropic hard magnetorheological elastomers. J. Mech. Phys. Solids 151, 104361.
Mushtaq, F., Torlakcik, H., Vallmajo-Martin, Q., Siringil, E.C., Zhang, J., Röhrig, C., Shen, Y., Yu, Y., Chen, X.-Z., Müller, R., et al., 2019. Magnetoelectric 3D scaffolds for enhanced bone cell proliferation. Appl. Mater. Today 16, 290–300.
Nair, M., Guduru, R., Liang, P., Hong, J., Sagar, V., Khizroev, S., 2013. Externally controlled on-demand release of anti-HIV drug using magneto-electric nanoparticles as carriers. Nature Commun. 4 (1), 1–8.
Nan, C.-W., Bichurin, M., Dong, S., Viehland, D., Srinivasan, G., 2008. Multiferroic magnetoelectric composites: Historical perspective, status, and future directions. J. Appl. Phys. 103 (3), 1.
Nan, C.W., Li, M., Feng, X., Yu, S., 2001a. Possible giant magnetoelectric effect of ferromagnetic rare-earth–iron-alloys-filled ferroelectric polymers. Appl. Phys. Lett. 78 (17), 2527–2529.
Nan, C.W., Li, M., Huang, J.H., 2001b. Calculations of giant magnetoelectric effects in ferroic composites of rare-earth–iron alloys and ferroelectric polymers. Phys. Rev. B 63 (14), 144415.
Narita, F., Fox, M., 2018. A review on piezoelectric, magnetostrictive, and magnetoelectric materials and device technologies for energy harvesting applications. Adv. Eng. Mater. 20 (5), 1700743.
Nguyen, T., Gao, J., Wang, P., Nagesetti, A., Andrews, P., Masood, S., Vriesman, Z., Liang, P., Khizroev, S., Jin, X., 2021. In vivo wireless brain stimulation via non-invasive and targeted delivery of magnetoelectric nanoparticles. Neurotherapeutics 1–16.
Osaretin, I.A., Rojas, R.G., 2010. Theoretical model for the magnetoelectric effect in magnetostrictive/piezoelectric composites. Phys. Rev. B 82 (17), 174415.
Palneedi, H., Maurya, D., Geng, L.D., Song, H.-C., Hwang, G.-T., Peddigari, M., Annapureddy, V., Song, K., Oh, Y.S., Yang, S.-C., et al., 2018. Enhanced self-biased magnetoelectric coupling in laser-annealed Pb (Zr, Ti) O3 thick film deposited on Ni foil. ACS Appl. Mater. Interfaces 10 (13), 11018–11025.
Peng, J., Witting, I., Geisendorfer, N., Wang, M., Chang, M., Jakus, A., Kenel, C., Yan, X., Shah, R., Snyder, G., et al., 2019. 3D extruded composite thermoelectric threads for flexible energy harvesting. Nature Commun. 10 (1), 1–8.
Pradhan, D.K., Kumari, S., Rack, P.D., 2020. Magnetoelectric composites: Applications, coupling mechanisms, and future directions. Nanomaterials 10 (10), 2072.
Psarra, E., Bodelot, L., Danas, K., 2019. Wrinkling to crinkling transitions and curvature localization in a magnetoelastic film bonded to a non-magnetic substrate. J. Mech. Phys. Solids 133, 103734.
Pyatakov, A.P., Zvezdin, A.K., 2012. Magnetoelectric and multiferroic media. Phys.-Usp. 55 (6), 557.
Rahmati, A.H., Liu, L., Sharma, P., 2022. Homogenization of electrets with ellipsoidal microstructure and pathways for designing piezoelectricity in soft materials. Mech. Mater. 173, 104420.
Rahmati, A.H., Yang, S., Bauer, S., Sharma, P., 2019. Nonlinear bending deformation of soft electrets and prospects for engineering flexoelectricity and transverse (d 31) piezoelectricity. Soft Matter 15 (1), 127–148.
Rivlin, R., 1949. Large elastic deformations of isotropic materials. V. The problem of flexure. Proc. R. Soc. Lond. Ser. A Math. Phys. Eng. Sci. 195 (1043), 463–473.
Rogers, J.A., Someya, T., Huang, Y., 2010. Materials and mechanics for stretchable electronics. Science 327 (5973), 1603–1607.
Ryu, J., Carazo, A.V., Uchino, K., Kim, H.-E., 2001a. Magnetoelectric properties in piezoelectric and magnetostrictive laminate composites. Japan. J. Appl. Phys. 40 (8R), 4948.
Ryu, J., Priya, S., Carazo, A.V., Uchino, K., Kim, H.-E., 2001b. Effect of the magnetostrictive layer on magnetoelectric properties in lead zirconate titanate/terfenol-D laminate composites. J. Am. Ceram. Soc. 84 (12), 2905–2908.
Schmid, H., 1994. Multi-ferroic magnetoelectrics. Ferroelectrics 162 (1), 317–338.
Shi, B., Li, Z., Fan, Y., 2018. Implantable energy-harvesting devices. Adv. Mater. 30 (44), 1801511.
Spaldin, N., Ramesh, R., 2019. Advances in magnetoelectric multiferroics. Nature Mater. 18, 203–212.
Srinivasan, G., Rasmussen, E., Hayes, R., 2003. Magnetoelectric effects in ferrite-lead zirconate titanate layered composites: The influence of zinc substitution in ferrites. Phys. Rev. B 67 (1), 014418.
Tan, K., Wen, X., Deng, Q., Shen, S., Liu, L., Sharma, P., 2020a. Soft rubber as a magnetoelectric material—Generating electricity from the remote action of a magnetic field. Materialstoday.
Tan, K., Wen, X., Gong, X., Deng, Q., Shen, S., 2020b. Diversifying temporal responses of magnetoactive elastomers. Mater. Res. Express 7 (4).
Tokura, Y., Seki, S., Nagaosa, N., 2014. Multiferroics of spin origin. Rep. Progr. Phys. 77 (7), 076501.
Torbati, M., Mozaffari, K., Liu, L., Sharma, P., 2022. Coupling of mechanical deformation and electromagnetic fields in biological cells. Rev. Modern Phys. 94 (2), 025003.
Toupin, R., 1960. Stress tensors in elastic dielectrics. Arch. Ration. Mech. Anal. 5 (1), 440–452.
Vopson, M., Fetisov, Y., Caruntu, G., Srinivasan, G., 2017. Measurement techniques of the magneto-electric coupling in multiferroics. Materials 10 (8), 963.
Wang, Y., Hu, J., Lin, Y., Nan, C.-W., 2010. Multiferroic magnetoelectric composite nanostructures. NPG Asia Mater. 2 (2), 61–68.
Wu, S., Eichenberger, J., Dai, J., Chang, Y., Ghalichechian, N., Zhao, R.R., 2022. Magnetically actuated reconfigurable metamaterials as conformal electromagnetic filters. Adv. Intell. Syst. 2200106.
Wu, S., Hu, W., Ze, Q., Sitti, M., Zhao, R., 2020. Multifunctional magnetic soft composites: A review. Multifunctional Mater. 3 (4), 042003.
Yang, S., Zhao, X., Sharma, P., 2017. Avoiding the pull-in instability of a dielectric elastomer film and the potential for increased actuation and energy harvesting. Soft Matter 13 (26), 4552–4558.

Ze, Q., Kuang, X., Wu, S., Wong, J., Montgomery, S.M., Zhang, R., Kovitz, J.M., Yang, F., Qi, H.J., Zhao, R., 2020. Magnetic shape memory polymers with integrated multifunctional shape manipulation. Adv. Mater. 32 (4), 1906657.

Ze, Q., Wu, S., Nishikawa, J., Dai, J., Sun, Y., Leanza, S., Zemelka, C., Novelino, L.S., Paulino, G.H., Zhao, R.R., 2022. Soft robotic origami crawler. Sci. Adv. 8 (13), eabm7834.

Zhai, J., Dong, S., Xing, Z., Li, J., Viehland, D., 2006. Giant magnetoelectric effect in Metglas/polyvinylidene-fluoride laminates. Appl. Phys. Lett. 89 (8), 083507.

Zhang, X., Ai, J., Ma, Z., Yin, Y., Zou, R., Su, B., 2020. Liquid metal based stretchable magnetoelectric films and their capacity for mechanoelectrical conversion. Adv. Funct. Mater. 30 (45), 2003680.

Zhang, X., Ai, J., Zou, R., Su, B., 2021a. Compressible and stretchable magnetoelectric sensors based on liquid metals for highly sensitive, self-powered respiratory monitoring. ACS Appl. Mater. Interfaces 13 (13), 15727–15737.

Zhang, Y., Chen, S., Xiao, Z., Liu, X., Wu, C., Wu, K., Liu, A., Wei, D., Sun, J., Zhou, L., et al., 2021b. Magnetoelectric nanoparticles incorporated biomimetic matrix for wireless electrical stimulation and nerve regeneration. Adv. Healthcare Mater. 2100695.

Zhang, J., Ping, L., Wen, Y., Wei, H., Lu, C., 2013. Giant self-biased magnetoelectric response with obvious hysteresis in layered homogeneous composites of negative magnetostrictive material samfenol and piezoelectric ceramics. Appl. Phys. Lett. 103 (20), 1062.

Zhao, R., Kim, Y., Chester, S.A., Sharma, P., Zhao, X., 2019. Mechanics of hard-magnetic soft materials. J. Mech. Phys. Solids 124, 244–263.

Zhao, X., Suo, Z., 2008. Method to analyze programmable deformation of dielectric elastomer layers. Appl. Phys. Lett. 93 (25), 251902.

Zhao, Z., Zhang, X.S., 2022. Topology optimization of hard-magnetic soft materials. J. Mech. Phys. Solids 158, 104628.

Zhou, Y., Maurya, D., Yan, Y., Srinivasan, G., Quandt, E., Priya, S., 2015. Self-biased magnetoelectric composites: An overview and future perspectives. Energy Harvest. Syst. 3.